A bistable autoregulatory module in the developing embryo commits cells to binary expression fates

Highlights

- Bistable network motifs have been proposed to stabilize cell fate commitment

- This hypothesis is tested in the context of *ftz* expression fate in fly embryos

- Live imaging is used to quantitively measure all parameters in a mathematical model

- Theory-experiment demonstrates that bistability mediates *ftz* expression fate

Authors

Jiaxi Zhao, Mindy Liu Perkins,
Matthew Norstad, Hernan G. Garcia

Correspondence

hggarcia@berkeley.edu

In brief

Bistability has been hypothesized to stabilize cellular expression fates. Zhao and Perkins et al. test this hypothesis using live imaging and theoretical modeling and reveal that *ftz* expression fate is bistable in fly development. This work sets the stage for quantitatively and predictively dissecting cellular decision-making in development.

Article

A bistable autoregulatory module in the developing embryo commits cells to binary expression fates

Jiaxi Zhao,[1,8] Mindy Liu Perkins,[2,8] Matthew Norstad,[3,7] and Hernan G. Garcia[1,3,4,5,6,9,*]
[1]Department of Physics, University of California, Berkeley, Berkeley, CA 94720, USA
[2]Developmental Biology Unit, European Molecular Biology Laboratory, 69117 Heidelberg, Germany
[3]Department of Molecular and Cell Biology, University of California, Berkeley, Berkeley, CA 94720, USA
[4]Biophysics Graduate Group, University of California, Berkeley, Berkeley, CA 94720, USA
[5]Institute for Quantitative Biosciences-QB3, University of California, Berkeley, Berkeley, CA 94720, USA
[6]Chan Zuckerberg Biohub – San Francisco, San Francisco, CA 94158, USA
[7]Present address: Bioethics Program, University of California, San Francisco, San Francisco, CA 94143, USA
[8]These authors contributed equally
[9]Lead contact
*Correspondence: hggarcia@berkeley.edu
https://doi.org/10.1016/j.cub.2023.06.060

SUMMARY

Bistable autoactivation has been proposed as a mechanism for cells to adopt binary fates during embryonic development. However, it is unclear whether the autoactivating modules found within developmental gene regulatory networks are bistable, unless their parameters are quantitatively determined. Here, we combine *in vivo* live imaging with mathematical modeling to dissect the binary cell fate dynamics of the fruit fly pair-rule gene *fushi tarazu* (*ftz*), which is regulated by two known enhancers: the early (non-autoregulating) element and the autoregulatory element. Live imaging of transcription and protein concentration in the blastoderm revealed that binary Ftz fates are achieved as Ftz expression rapidly transitions from being dictated by the early element to the autoregulatory element. Moreover, we discovered that Ftz concentration alone is insufficient to activate the autoregulatory element, and that this element only becomes responsive to Ftz at a prescribed developmental time. Based on these observations, we developed a dynamical systems model and quantitated its kinetic parameters directly from experimental measurements. Our model demonstrated that the *ftz* autoregulatory module is indeed bistable and that the early element transiently establishes the content of the binary cell fate decision to which the autoregulatory module then commits. Further *in silico* analysis revealed that the autoregulatory element locks the Ftz fate quickly, within 35 min of exposure to the transient signal of the early element. Overall, our work confirms the widely held hypothesis that autoregulation can establish developmental fates through bistability and, most importantly, provides a framework for the quantitative dissection of cellular decision-making.

INTRODUCTION

One of the central questions in developmental biology concerns how cells precisely and irreversibly adopt distinct cellular fates. It has been argued that cells assume their unique gene expression profiles through a sequence of decisions among branching paths,[1,2] famously encapsulated by "Waddington's landscape" of peaks and valleys delineating the possible trajectories that a cell can follow.[3] Genetic networks that lock a cell into one of these trajectories may be thought of as "memory modules" that guide cells through valleys in the landscape to their ultimate fates. In the simplest case, where a decision is made between two alternative developmental fates, the memory module is binary and referred to as a switch. The state of the switch is set by the action of transient upstream regulatory signals.

Several genetic motifs, including autoactivation and mutual repression, are capable of maintaining binary cell fates.[4,5]

However, the mere presence of these motifs is insufficient to guarantee that a network can remember its expression state once upstream regulators have degraded. The ability to lock onto high or low expression levels results from bistability (see "A primer on bistability" in STAR Methods), a systems-level property that depends upon the quantitative details of the kinetics of the involved chemical reactions.[6–8]

Though bistability is widely invoked to explain cell fate decisions,[5] relatively little quantitative data exist to confirm bistability in gene expression modules within developing embryos. Previous studies in cell culture and fixed embryos have provided evidence for bistability in hematopoietic differentiation,[9,10] the Shh network,[11] the vertebrate hindbrain,[12] between the BMP and FGF morphogens,[13] and within the Notch-Delta signaling system.[14] Quantitative evidence for multistability in fruit fly embryos has also been derived from fitting the parameters of high-dimensional network models to fixed tissue measurements.[15–20] While

A upstream regulatory factors   early protein   late protein

B developmental time

expression from
early module

Case 1: Bistable (memory)

expression from
autoregulatory module

total expression
(early + autoregulatory)

permanent pattern
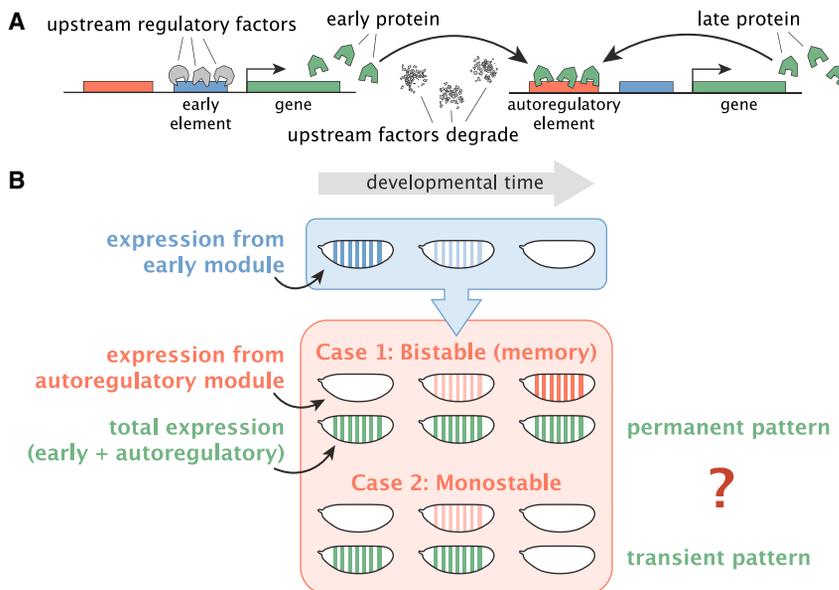
Case 2: Monostable

?

transient pattern

Figure 1. The bistability of the autoregulatory module can determine cell fate

(A) The autoregulatory architecture consists of an early element to which upstream factors bind to transiently upregulate gene expression of an activator and an autoregulatory element to which the activator binds to, under certain circumstances, promote its own expression even once the upstream factors have degraded.

(B) The total activator concentration (green) is a sum of the protein produced by the early (blue) and autoregulatory (red) modules. If the autoregulatory module is bistable, it possesses binary memory that permits transiently high concentrations of early protein to be locked into permanent high expression levels (high cell fate) as shown in Case 1. If, in contrast, the autoregulatory module is monostable, then it may transiently boost protein levels from the early module, but over time all cells will ultimately revert to the same low fate as depicted in Case 2.

these models are capable of reproducing the observed phenomenology, there is no guarantee that the optimal set of inferred parameter values reflects actual biophysical quantities.[21–24] Thus, it is important to verify that the conclusions drawn from computational modeling and *in vitro* experiments apply to developmental systems *in vivo* in the context of models that quantitatively capture the molecular interactions that underlie cellular decision-making. To the best of our knowledge, evidence for the bistability of a genetic module based on these molecular interactions in an intact multicellular organism has not yet been demonstrated.

The early development of the fruit fly *Drosophila melanogaster* is an ideal model system for studying binary cell fate determination, due to the presence of pair-rule genes such as *fushi tarazu* (*ftz*) that form discrete stripes at the cellular blastoderm stage prior to gastrulation (2.5–3.5 h after fertilization[25–29]). The expression of *ftz* is regulated by two main enhancers: the early, or zebra, element and the autoregulatory element[30] (Figures 1A and S1). The early element responds to upstream transcription factors such as the gap genes to establish the initial expression pattern of seven stripes.[31] This element is functionally distinct from the autoregulatory element, which contains multiple Ftz binding sites that allow Ftz to activate its own expression[32–34] (Figure S1). This autoactivation network motif is theoretically capable of exhibiting bistability and has therefore been hypothesized to act as a binary memory module.[4,35]

Whether a cell possesses a memory module determines whether observed states of gene expression are transient in the absence of continued external signaling, or whether these states can be locked into permanent cell fates that can be maintained without further intervention. Specifically, if the autoregulatory module is bistable, then it maintains high *ftz* expression driven by the transient presence of upstream factors (Figure 1B, case 1), even once those factors degrade (or until further regulatory mechanisms intervene). If, instead, the autoregulatory element is monostable, then the observed

separation of Ftz concentration into high and low levels persists only as long as upstream factors are present to regulate expression. In their absence, Ftz expression would revert to a single fate for all cells (Figure 1B, case 2). It is important to note, however, that in this case, the transiently high or low trajectory of Ftz concentration could still be instructive for regulating downstream genes.

Here, we characterize the *ftz* autoregulatory module *in vivo* through quantitative real-time measurements in living fruit fly embryos. Focusing on stripe 4 expression, we observe that Ftz expression separates into discrete high and low levels at the blastoderm stage during the 20 min prior to gastrulation, concurrent with a transition in regulatory control from the early to the autoregulatory element. We discover that autoregulation is triggered at a specific time point in development—presumably through the action of "timer genes"[36–38]—rather than through a readout of Ftz concentration alone. Based on these observations, we develop a dynamical systems model and quantitate its parameters from simultaneous real-time measurements of *ftz* transcription and Ftz protein dynamics in single cells of living embryos. Our model predicts binary Ftz expression levels at gastrulation with high accuracy and demonstrates that, indeed, the *ftz* autoregulatory module is bistable. We conclude that the *ftz* autoregulatory element acts as a memory module to commit cells to binary fates that are otherwise transiently defined by the early element, thereby validating a long-standing hypothesis in developmental and systems biology that bistability underlies cell fate determination. Simulations further make it possible to quantitatively define a developmental commitment window, which shows that the autoregulatory module requires about half an hour to establish a memory of the transient signal from the early module. Thus, our work provides a framework for the dissection of other regulatory modules in the gene regulatory networks that dictate development based on this interplay between dynamical systems models and real-time experiments.
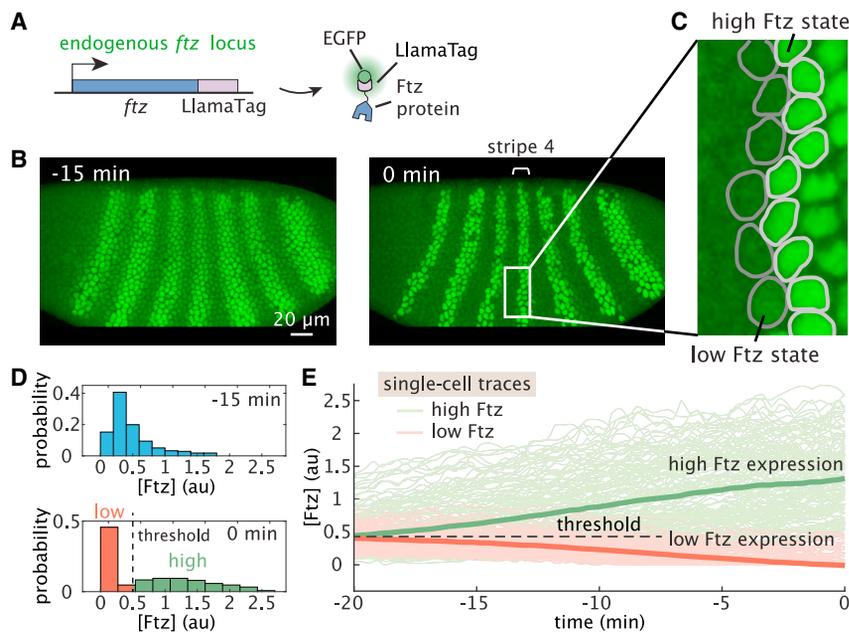
Figure 2. Binary cell states are rapidly established prior to gastrulation

(A) A fusion of endogenous Ftz to a LlamaTag visualizes highly dynamic Ftz protein patterning in the early fly embryo. Once Ftz protein is translated in the cytoplasm, LlamaTag binds to maternally deposited EGFP and is transported into the nucleus, increasing nuclear fluorescence to produce a direct readout of Ftz concentration.

(B) Snapshots from a video capturing Ftz concentration dynamics. The embryo is oriented with the anterior toward the left. Time is given relative to gastrulation.

(C) Ftz expression along the anterior boundary of stripe 4 shows a discrete transition between cell states.

(D) Histograms of single-nucleus fluorescence values at different developmental time points show that a threshold can be used to classify cells into high Ftz and low Ftz cell states at gastrulation.

(E) Single-cell trajectories of nuclei at the anterior boundaries of Ftz stripe 4. Green and red lines are averages for nuclei determined to have high and low Ftz levels at gastrulation, respectively, as defined in (D).

See also Video S1.

RESULTS

Binary *ftz* expression states are established in early development

To understand the role of autoactivation in deciding Ftz expression levels, we first visualized Ftz protein dynamics over time. We used CRISPR-mediated recombination[39] to fuse a LlamaTag, a fluorescent probe that reports on the fast protein dynamics that characterize early embryonic development, to the C terminus of the endogenous Ftz protein[40] (Figure 2A). An examination of the fluorescently labeled Ftz protein in the early embryo shows that, around 15 min before gastrulation, Ftz protein is expressed in a seven-stripe pattern with clear, smooth boundaries (Figure 2B, left). This expression pattern refines over the following 15 min into sharp stripe boundaries by the start of gastrulation (Figure 2B, right). The result shows that cells express either high or low levels of Ftz protein, as pictured in Figure 2C for the anterior boundary of stripe 4, consistent with results from previous studies.[40–42] Note that, throughout this work, we focus on the anterior boundary of stripe 4 because it is the only Ftz stripe that has been demonstrated to be driven exclusively by the early and autoregulatory elements and not by other enhancers in the gene's vicinity[41] (Figure S1).

Our live imaging measurements allowed us to quantitatively examine the dynamics with which binary cell states are established by calculating the Ftz protein distribution in individual nuclei at different time points in development (Figure 2D). Our analysis revealed that the expression level is initially unimodal across all cells (Figures 2D, top, and 2E) and then evolves into a bimodal distribution within 15 min (Figures 2D, bottom, and 2E). Consistent with our qualitative observations in Figures 2B and 2C, cells at these later times can be quantitatively classified into distinct "high-Ftz" and "low-Ftz" cell states using a single threshold chosen by a visual inspection of the distribution (Figures 2D, bottom, and 2E), which indicates that binary cell states are already established prior to the onset of gastrulation. Moreover, though the two cell states are clearly distinguishable from each other, there is significant cell-to-cell variability within the high-Ftz state (Figures 2D, bottom, and 2E).

Previous studies have established that autoregulation plays a key role during *ftz* expression: a lack of the *ftz* autoregulatory element or mutated Ftz binding sites within the element results in the loss of Ftz expression at later developmental stages.[30,33] However, it is unclear at what developmental time *ftz* autoregulation is initiated in response to the Ftz expression stemming from the early element. Specifically, is the autoregulatory element active before stripes of Ftz expression emerge, or is autoregulation invoked after the early element has already established this pattern? To distinguish between these two scenarios, we decoupled the transcriptional dynamics driven by the early and autoregulatory elements by creating two separate reporter constructs, each containing only the early or autoregulatory elements followed by MS2 stem-loops that enable the direct visualization of transcriptional dynamics[43,44] (Figures 3A and S1). All constructs were inserted in the same genomic location.

We observed that the early element already drives a relatively constant gene expression level around 20 min prior to gastrulation (Figures 3B and 3C). Then, at 15 min before gastrulation, its transcriptional activity decreases significantly, resulting in a 50% reduction within the next 20 min of development (Figures 3B and 3C). Conversely, autoregulation is initiated 20 min prior to gastrulation, with its activity increasing until gastrulation starts (Figure 3C). This transition between the early and autoregulatory elements occurs while binary cell states are being established (Figure 2).

ftz autoactivation is triggered at a specific developmental time

Previous studies have established that *ftz* is autoactivated through a specialized enhancer referred to as the autoregulatory
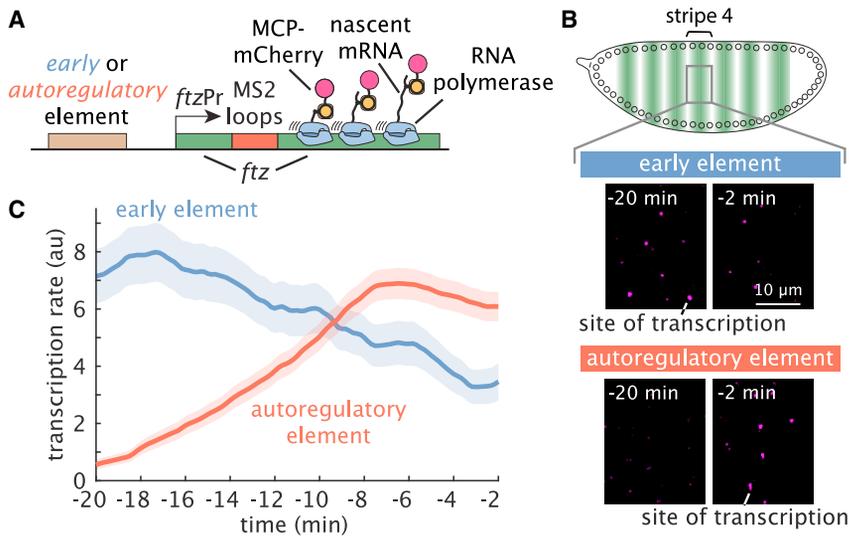
Figure 3. A sequential transition in Ftz regulation from the early to the autoregulatory element occurs while discrete cell states are established

(A) Imaging transcriptional dynamics of the early and autoregulatory elements using the MS2 system. Maternally deposited MS2 coat protein (MCP) fused to mCherry binds to MS2 stem-loops in the nascent RNA of the reporter construct.

(B) Snapshots of sites of nascent transcript formation labeled by MS2 from reporters of the early and autoregulatory elements at different time points. Transcription from the early element decreases, while transcription from the autoregulatory element increases shortly before gastrulation.

(C) Quantification of the transcriptional activity reported by the MS2 fluorescence from the early (n = 3 embryos) and autoregulatory (n = 6 embryos) elements as a function of time confirms that, within 20 min, *ftz* gene expression transitions from originating mainly from the early element to being dominated by the autoregulatory element. MS2 traces are smoothed using a moving average of 5 min. The transcription rate is calculated from the measured MS2 signal, which is an approximation of the mRNA production rate.[40,43,45] Shaded region indicates standard errors over multiple embryos.

See also Figure S1.

element.[30,32–34] The autoregulatory element cannot drive transcription in the absence of Ftz protein, but it is unclear whether the mere presence of high Ftz concentrations is sufficient to initiate autoactivation, or whether other factors must also be present to trigger the observed transition in *ftz* expression between the early and autoregulatory elements (Figure 3C).

To further investigate the nature of the regulatory transition that initiates autoactivation, we quantified the gene regulatory function of the *ftz* autoregulatory element at distinct developmental times. The gene regulatory function—also called the input-output function—describes the relationship between Ftz protein concentration and the rate of *ftz* transcription driven by the autoregulatory element. Since Ftz is autoactivating, we expect the gene regulatory function to be S-shaped (i.e., sigmoidal), with no transcription in the absence of Ftz protein, a steep increase in transcription as Ftz levels approach a "threshold" level, and maximal transcription for high concentrations of Ftz. If Ftz protein is the only factor that regulates transcription levels from the autoregulatory element, then the gene regulatory function should remain unchanged even as the concentrations of other regulatory factors evolve over time; that is, a fixed concentration of Ftz protein should correspond to the same transcription rate regardless of the time of measurement. Alternatively, if other time-varying factors also contribute to *ftz* expression from the autoregulatory element, then we expect the gene regulatory function to change over time such that the same level of Ftz protein will drive different levels of transcription depending on developmental time.

We measured the gene regulatory function of the autoregulatory element at different time points by constructing an experimental system that permits simultaneous monitoring of input Ftz concentration and corresponding output transcriptional dynamics driven by the autoregulatory element. We used tagged endogenous Ftz protein as the input and introduced a transgenic reporter with MS2 loops under the control of the *ftz*

autoregulatory element as the output (Figure 4A). To prevent the reporter from expressing unlabeled Ftz protein, which could feed back into the autoregulatory element and interfere with the measurement of the gene regulatory function, we created a new autoregulatory construct by combining the *ftz* autoregulatory element with the coding region of the *yellow* gene. Control experiments confirmed that the autoregulatory constructs used in Figures 3 and 4 show the same temporal dynamics prior to gastrulation (Figure S2). Live imaging of the anterior boundary of Ftz stripe 4 showed that, initially, around 25 min prior to gastrulation, both Ftz expression and the autoregulatory response were relatively low, and later increased as development progressed (Figure 4B). Just before gastrulation, the Ftz protein pattern refined into a discrete boundary, with the *ftz* autoregulatory response clearly following the stripe boundary (Figure 4B).

To calculate the regulatory function, we restricted our analysis to the cells at the anterior boundary of stripe 4 as a means to minimize the influence of other position-dependent transcription factors that might also contribute to *ftz* autoactivation.[34] We first extracted two rows (high and low) of boundary cells. Then, we separated the input Ftz concentration and output transcription from the autoregulatory element in the data corresponding to each individual cell (Figure 4C) into ten quantiles and fit a Hill function to the quantile averages to get the gene regulatory function of *ftz* autoregulation within a defined temporal range (for example, −10 min to −5 min for Figure 4D). Our analysis revealed a sharp regulatory relationship between Ftz concentration and autoregulatory response shortly before gastrulation, with a Hill coefficient of 3.3 ± 0.8 (Figure 4D). Such a Hill coefficient is comparable to those estimated in the context of autoactivation in vertebrate hindbrain development[12] as well as those observed in simpler regulatory motifs that do not feature feedback.[46]

We repeated the process described above at multiple developmental times to measure the temporal dynamics of the
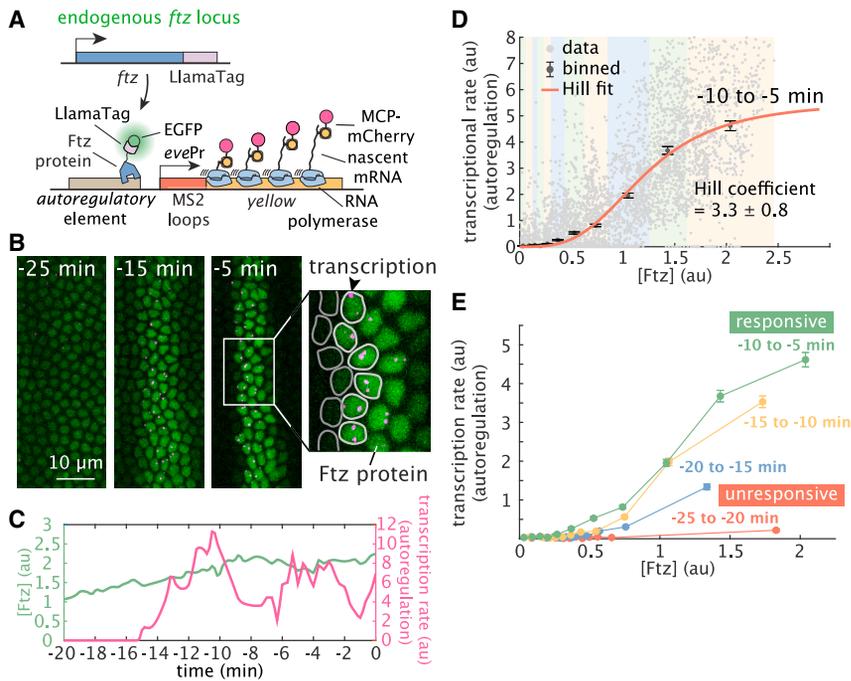
Figure 4. Two-color live imaging reveals that *ftz* autoregulation is initiated at a specific developmental time

(A) Two-color tagging enables simultaneous visualization of input Ftz concentration using LlamaTag and output autoregulatory transcriptional dynamics using a reporter carrying the MS2 system.

(B) Representative frames from live-imaging data. Green and magenta channels correspond to Ftz concentration and transcriptional output from the *ftz* autoregulatory element, respectively. Outlines indicate cells expressing high (light gray) or low (dark gray) levels of Ftz protein.

(C) Illustrative single-cell trace of Ftz and autoregulatory activity. Green and magenta lines correspond to the Ftz protein and transcriptional activity of the autoregulatory element, respectively. Both protein and MS2 traces are smoothed using a moving average of 1 min.

(D) Experimentally measured gene regulatory function of the *ftz* autoregulatory element between −10 min and −5 min relative to gastrulation. Gray points correspond to simultaneous measurements of Ftz and MS2 fluorescence at individual time points from single-cell traces at the anterior boundary of stripe 4 (n = 211 nuclei). These points were grouped into quantiles, and a Hill function (red line) was fit to the quantile means.

(E) The autoregulatory input-output function evolves over time, as the *ftz* autoregulatory element transitions from an unresponsive to a responsive state within 15 min, indicating that *ftz* autoregulation is initiated through a developmental time-based mechanism. The transcription rate is calculated from the measured MS2 signal, which is an approximation of the mRNA production rate.[40,43,45] Error bars shown indicate standard errors. All data are from n = 7 embryos.

See also Figure S2 and Video S2.

regulatory function for *ftz* autoactivation. The results, shown in Figure 4E, revealed that the regulatory function is clearly distinct at different time points. Around −25 min to −20 min, the *ftz* autoregulatory element drives almost no transcription regardless of Ftz concentration, as can be appreciated by the fact that the gene regulatory function is almost flat near 0 during this time interval (Figure 4E, red line). However, within 15 min, Ftz levels above a threshold of about 1 a.u. are sufficient to drive Ftz transcription from the autoregulatory element, with higher input Ftz concentrations resulting in progressively higher transcription rates at later times (Figure 4E, green line). The fact that Ftz levels above a threshold result in high transcription rates at gastrulation but produce no transcription −20 min earlier is a clear indicator that the autoregulatory element is not always equally responsive to input Ftz concentration. Instead, its capacity to drive *ftz* expression is enabled at a specific developmental time, presumably by upstream transcription factors.

Dynamical systems modeling of *ftz* regulation

The fact that Ftz can exhibit a high state at one point in time does not imply that this high state will persist in the absence of upstream regulation (Figure 1B). Determining whether the autoregulatory module is bistable requires turning the schematic in Figure 1A (including both early and autoregulatory elements) into an explicit dynamical systems model with empirically determined parameter values.

We begin by mathematically describing the expression dynamics driven by the *ftz* early enhancer. We assume that upstream regulators binding to the early enhancer dictate the transcription rate $r(t)$ (Figure 5A). Our measurements (Figures 3C, 5I,

and 5J; STAR Methods "Early element transcriptional activity decay rate β") revealed that, after the onset time for the autoregulatory enhancer $t_{on} = -20$ min (Figure 4E), $r(t)$ follows an approximately exponential decay with a decay constant $1/\beta$. This allows us to represent $r(t)$, the mRNA $R_{early}(t)$, and the protein $P_{early}(t)$ produced from the early module as

$$
\begin{cases}
\dfrac{dr}{dt} &= -\beta r(t) \\[2mm]
\dfrac{dR_{early}}{dt} &= \underbrace{r(t)}_{\text{synthesis}} - \underbrace{\gamma_R R_{early}(t)}_{\text{degradation}} \\[2mm]
\dfrac{dP_{early}}{dt} &= \underbrace{\alpha R_{early}(t)}_{\text{synthesis}} - \underbrace{\gamma_P P_{early}(t)}_{\text{degradation}}
\end{cases}
, \ t \geq t_{on} \quad \text{(Equation 1)}
$$

where α is the translation rate and γ_R and γ_P are the mRNA and protein degradation rates, respectively. Regardless of the choice of parameter values or initial conditions, all three quantities, $r(t)$, $R_{early}(t)$, and $P_{early}(t)$, converge to 0 as t goes to infinity (STAR Methods section "Early element"), indicating that the early module is monostable and signaling from upstream factors is transient. Since embryos at this stage in nc14 are undergoing cellularization and cell membranes have already formed, we assume that diffusion of mRNA and protein is negligible.[16,20,47]

As shown in Figure 4E, after the onset time t_{on}, the autoregulatory element becomes responsive to Ftz. Building on the simple model introduced in STAR Methods section "A primer on bistability," we describe the mRNA ($R_{late}(t)$) and protein ($P_{late}(t)$) dynamics dictated by this element as
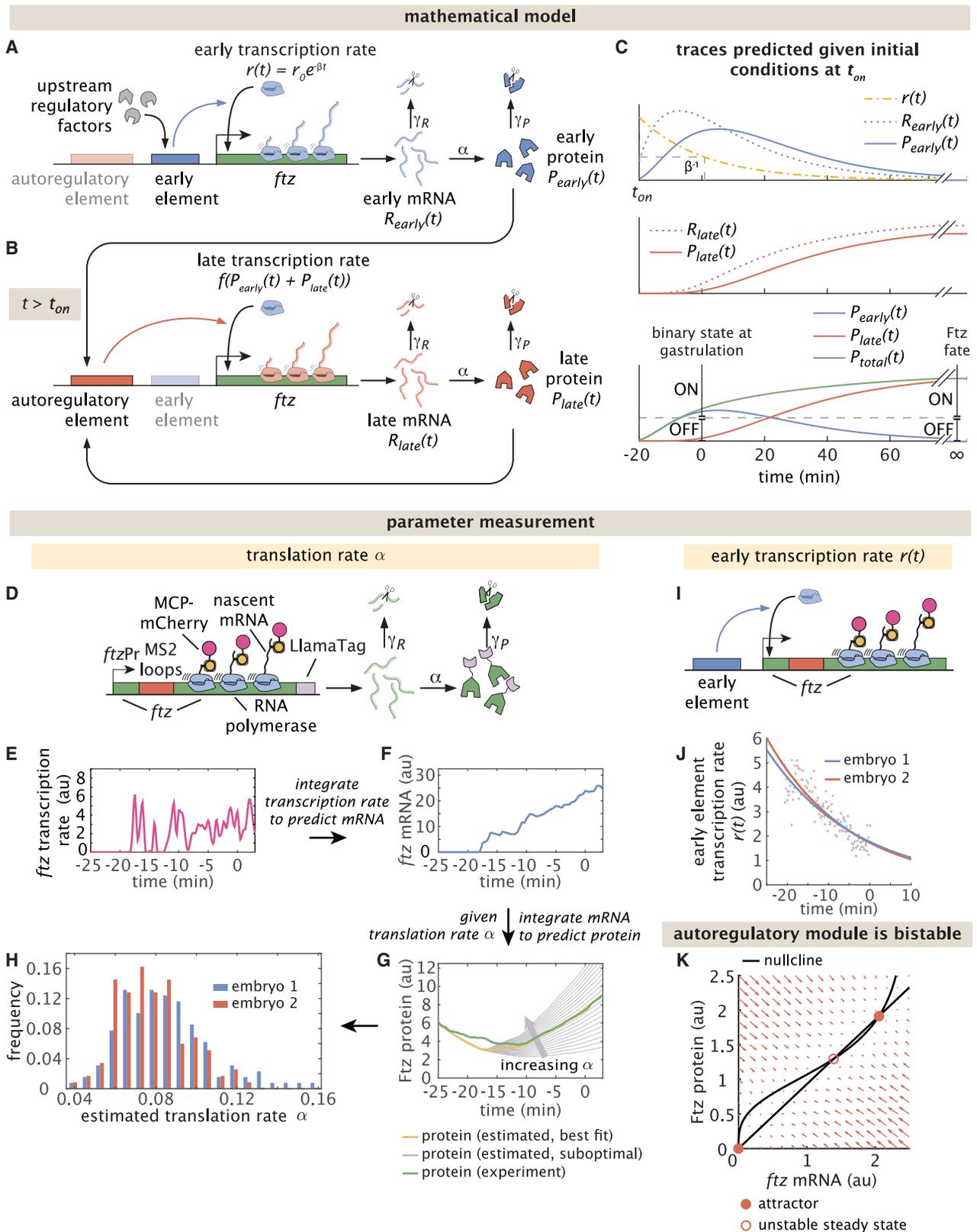
Figure 5. Quantifying dynamical systems model parameters reveals that *ftz* autoregulation is bistable

(A) The early element drives *ftz* transcription at a rate $r(t)$ that drops exponentially over time with rate β, producing early mRNA $R_{early}(t)$ that is translated at rate α into Ftz protein $P_{early}(t)$.

$$\begin{cases} \dfrac{dR_{late}}{dt} = \overbrace{cf\big(P_{early}(t) + P_{late}(t)\big)}^{\text{synthesis}} - \overbrace{\gamma_R R_{late}(t)}^{\text{degradation}} \\ \dfrac{dP_{late}}{dt} = \underbrace{\alpha R_{late}(t)}_{\text{synthesis}} - \underbrace{\gamma_P P_{late}(t)}_{\text{degradation}} \end{cases}, \ t \geq t_{on}.$$

(Equation 2)

Here, $f(P)$ is the gene regulatory function describing the output rate of mRNA production as a function of the total input Ftz concentration (the sum of the protein produced by the early and autoregulatory elements) as measured for the transgene in Figure 5B. Because $f(P)$ was measured for a transgene and not for the endogenous autoregulatory element, we also assume a scaling factor c. As indicated in Equation 2, we assume that the autoregulatory element is only active for $t \geq t_{on}$. Our model produced nearly identical results whether we assumed that this transition to full responsiveness occurred instantaneously at time t_{on} as shown here, or whether we assumed a gradual increase in responsiveness over time (STAR Methods section "Best predicted nuclei").

Given quantitative parameter values and initial conditions ($r(t_{on})$, $R_{early}(t_{on})$, and $P_{early}(t_{on})$), the full model for *ftz* regulation described by Equations 1 and 2 can be used to simulate the trajectory of total Ftz concentration in a nucleus over time. Specifically, we calculate Ftz expression levels (low or high) at gastrulation as well as at long times (i.e., $t \rightarrow \infty$). We will refer to the predicted stable concentration of Ftz at long times as the ultimate *fate* of the cell, in contrast to the (possibly transient) binary expression state at gastrulation (Figure 5C).

Quantifying model parameters shows that the autoregulatory module is bistable

The first step toward testing our model is to obtain numerical values for the parameters. The mRNA and protein decay rates γ_R and γ_P were drawn from existing measurements in the literature.[40,48] The gene regulatory function $f(P)$ was already measured as described in the previous section (Figure 4D). The

remaining free parameters (α, β, and c) were directly measured through a set of independent experiments.

First, we measured the translation rate α using a reporter transgene that combined MS2 and LlamaTag such that *ftz* transcription rate and Ftz concentration could be simultaneously measured (Figure 5D). We estimated $R(t)$, the total amount of mRNA produced by individual nuclei up until time t, by integrating the MS2 fluorescence over time[43] (Figure 5E and F). Next, we integrated $R(t)$ for different values of the translation rate α to estimate protein dynamics $P(t)$ (Figure 5G). We calculated the best-fitted α for each nucleus and averaged them for each embryo (Figure 5H). Averaging α over two embryos yielded $\alpha = 0.082 \pm 0.004$ protein/(mRNA·min) (Table S1). Second, we determined the decay rate β for transcription from the early element by fitting an exponential function to the average transcription dynamics of the early element construct within individual embryos (Figure 5I and J). Averaging the resulting decay rates per embryo resulted in $\beta = 0.0480 \pm 0.0021$ 1/min.

Using these parameters, together with the inferred scaling factor c (Figure S3; see STAR Methods section "Scaling factor c" for details), we analyzed the autoregulatory module and determined that it is indeed bistable once upstream regulatory factors have degraded and the early element ceases to contribute to transcription ($P_{early} = 0$). As illustrated by the phase portrait in Figure 5K (and introduced in STAR Methods section "A primer on bistability"), the nullclines intersect at three points that define two attractors separated by an unstable steady state. Thus, our model indicates that the *ftz* autoregulatory module is capable of maintaining high or low levels of *ftz* expression indefinitely, and hence that there are two fates for Ftz on long timescales. Which fate a cell ultimately adopts will therefore depend on the protein initially produced by the early module.

Ftz expression state is instructed by the early element rather than by the autoregulatory element

Our model does not only predict that the Ftz autoregulatory module acts as a bistable switch. Because no free parameters remain, given initial conditions to the system, the model can

---

(B) The autoregulatory element drives Ftz expression starting at time t_{on} with a rate determined by the gene regulatory function $f(P)$, where P is the total Ftz produced from both the early and autoregulatory modules, $P_{early} + P_{late}$.

(C) The model can be used to predict traces for the mRNA and protein concentrations over time based on initial transcription rates and molecular concentrations at t_{on}. We use the term "state" to refer to whether Ftz expression is high or low at gastrulation, and "fate" to refer to the total Ftz concentration at long timescales ($t = \infty$).

(D–H) Estimating the translation rate α.

(D) We used the Ftz-MS2-LlamaTag transgenic construct for estimating the translation rate α.

(E) Illustrative example of a single-cell raw MS2 trace that reports on the instantaneous *ftz* transcription rate. MS2 traces are smoothed using a moving average of 1 min. Ftz traces are smoothened using a moving average of 5 min.

(F) For a given value of mRNA degradation rate γ_R, we integrate the MS2 traces to estimate the mRNA dynamics in individual nuclei.

(G) For a given value of the translation rate α and known degradation rates γ_R and γ_P,[40,48] we integrate the estimated mRNA dynamics to predict Ftz dynamics in individual nuclei. We then choose the value of α that leads to the best agreement between our prediction (yellow line) and experiment (green line). Gray lines show suboptimal fits.

(H) Histogram distribution of best-fitted α values for individual cells within two embryos.

(I and J) Inferring the decay rate of the early element transcription rate β.

(I) The early element regulates the transcription rate $r(t)$. Construct design is the same as the one illustrated in Figure 3A.

(J) The exponential fit of early element transcription (n = 2 embryos). Gray dots represent the averaged early element transcription rate at individual time points from a single embryo. Red and blue lines are the exponential fits that are used to estimate the early element decay rate β.

(K) Given the measured model parameters, our model shows that the autoregulatory module is bistable. A phase portrait (as described in STAR Methods section "A primer on bistability") illustrates that the autoregulatory module represented by Equation 2 is bistable in the absence of early protein. This implies that the autoregulatory enhancer is capable of maintaining high or low levels of Ftz indefinitely. The transcription rate is calculated from the measured MS2 signal, which is an approximation of the mRNA production rate.[40,43,45] The numerical values of experimentally measured parameters are reported in Table S1.
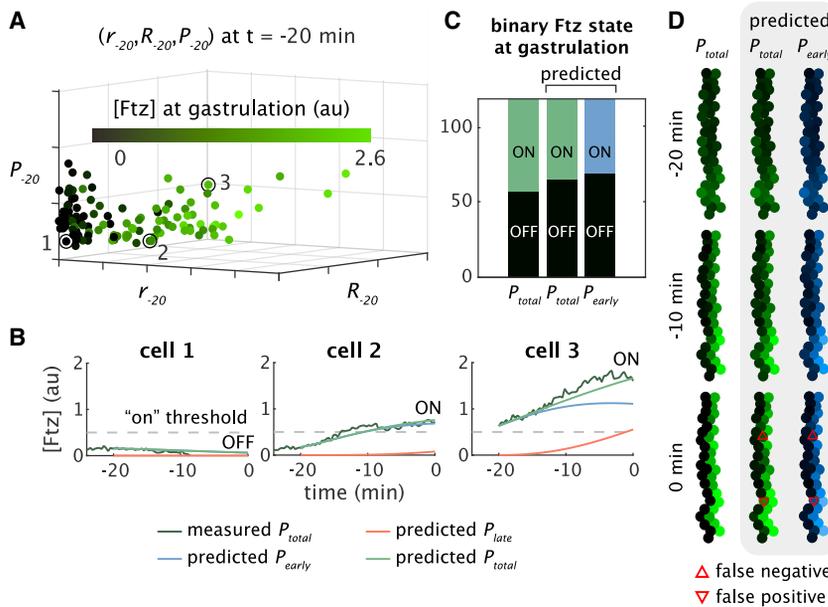
See also Figures S3 and S4.

Figure 6. Model reveals that the early element alone is sufficient to accurately predict binary Ftz expression states at gastrulation

(A) The mRNA production rate r_{-20}, mRNA concentration R_{-20}, and protein concentration P_{-20} from the early element are measured at 20 min before gastrulation for each nucleus (filled circle). These measurements are used to set the initial conditions for simulations of Ftz concentration at all times after t_{on} in each individual cell. Circle color corresponds to the measured total Ftz concentration at gastrulation.

(B) Measured (dark green) versus simulated (light green) total Ftz for three representative cells corresponding to the circled points in (A). We can classify a nucleus as in the high Ftz state (ON) or the low Ftz state (OFF) at gastrulation ($t = 0$ min) depending on whether the total Ftz levels are above or below the empirically identified threshold (gray dashed line) (Figure 2D). Predicted simulated traces are also shown for early (blue) and late (red) Ftz contributions. Note that, for cell 2, the blue and green curves substantially overlap.

(C) Measured fraction of cells in the ON or OFF expression state at gastrulation (left) compared to predictions based on thresholding total Ftz (center)

or early Ftz alone (right). Predictions using total Ftz concentration or Ftz produced by the early element lead to similar accuracy in comparison to empirical results (total Ftz, 102 of 118 nuclei; early Ftz, 100 of 118 nuclei).

(D) Results from a representative embryo show that the experimentally measured stripe pattern (left) is recapitulated by simulation (middle). A stripe pattern is still evident at gastrulation even from the predicted early Ftz concentration alone (right). Nuclear intensities at all time points are normalized to the predicted steady-state high Ftz concentration. Red triangles denote nuclei predicted to be ON that were OFF (downward) and nuclei predicted to be OFF that were empirically ON (upward). Parameters for all simulations were experimentally measured as reported in the main text; numerical values are reported in Table S1.

See also Figures S5 and S6.

also predict how Ftz concentration changes over time. Therefore, a critical test for the accuracy of the model is whether it can predict Ftz expression state at gastrulation.

To predict Ftz dynamics, we measured the initial transcription rate ($r(t_{on}) = r_{-20}$), mRNA level ($R_{early}(t_{on}) = R_{-20}$), and protein level ($P_{early}(t_{on}) = P_{-20}$) from the early module at the onset time $t_{on} = -20$ min (Figure 6A) in embryos expressing endogenous Ftz labeled with LlamaTag (Figure 2A; STAR Methods section "Extracting initial conditions"). Since, prior to onset, the autoregulatory element has not yet produced any mRNA or protein, knowing these three initial conditions is sufficient to calculate the trajectory for total Ftz concentration $P_{total}(t) = P_{early}(t) + P_{late}(t)$ within the corresponding nucleus using our model (Figure 6B).

For each simulated trajectory, we determined binary Ftz expression state at gastrulation based on whether total Ftz concentration exceeded the threshold empirically determined in Figure 2D, as shown in Figure 6B. Comparing our predictions and experimental measurements revealed that our model predicts binary Ftz expression state at gastrulation with an accuracy of 86.4% (102 of 118 nuclei) across n = 3 embryos (Figure 6C). The majority of classification errors were derived from a single embryo, with stochastic simulations suggesting the remainder may be attributed to noisy gene expression dynamics (STAR Methods section "Stochastic simulations"; Figure S6). Thus, our model appears to capture the essential deterministic components of Ftz dynamics.

While it is clear that the autoregulatory element establishes developmental memory of Ftz expression over long timescales, our simulations show that a stripe pattern is already evident at gastrulation from the contribution of the early protein alone,

ignoring the autoregulatory contribution (Figure 6D). Indeed, predictions of Ftz state at gastrulation based on thresholding the early protein concentration alone were 84.7% accurate (100 of 118 nuclei)—only 1.7% less accurate than when the autoregulatory contribution is also taken into account (Figure 6C). Thus, it appears that the anterior boundary of stripe 4 at gastrulation is predominantly defined by the regulatory activity of upstream factors binding the early element independent of autoregulatory activity. This result supports the conclusion that the autoregulatory module primarily serves to commit cells to fates predetermined by the early element.

Ultimate Ftz fate is robustly specified in half an hour

Although the autoregulatory element becomes active 20 min before gastrulation, our model suggests that Ftz expression state at gastrulation is nevertheless primarily determined by the early element. It is therefore conceivable that some cells transiently express high Ftz at gastrulation without committing to stably expressing high Ftz in the long term. To explore this possibility, we compared the binary classification of nuclei at gastrulation with the final high or low expression fate predicted by the model at long timescales. Specifically, we analyzed a subset of nuclei, which we call the "best predicted nuclei," whose quantitative expression levels—including their expression state at gastrulation—were successfully predicted using our model (Figures 6C and 6D; STAR Methods section "Best predicted nuclei"). We found that 93.7% (74 of 79 nuclei) were predicted to maintain their binary state at gastrulation and adopt the corresponding Ftz expression fate in steady state (e.g., cell 3 in Figure 7A). The remaining 6.3% of nuclei (5 of 79), despite having
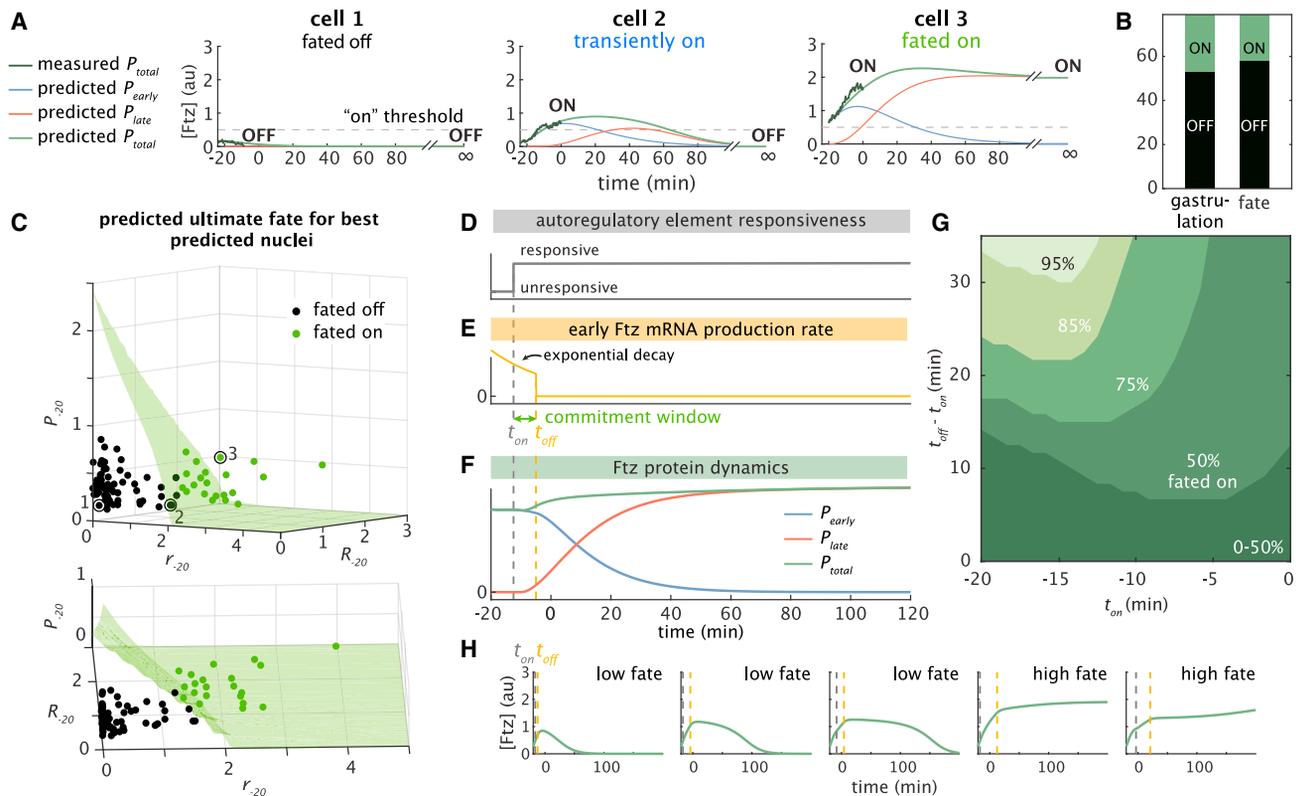
Figure 7. *In silico* analysis reveals the window of commitment of cells to Ftz fate

(A) Simulated Ftz concentration over long timescales (total, light green; early, blue; late, red) for the same cells shown in Figure 6B (circled again here in C). Empirical measurements until gastrulation are plotted in dark green for comparison.

(B) Bar charts for the best predicted subset of nuclei (n = 79; STAR Methods section "Best predicted nuclei") show that most analyzed cells are predicted to adopt an ultimate fate (right) that matches the measured binary Ftz expression state at gastrulation (left).

(C) The switching separatrix (green surface) separates nuclei predicted to adopt the high Ftz fate (green circles above the surface) from those predicted to adopt the low Ftz fate (black circles below the surface) given their initial conditions. Top and bottom subpanels show the same plot from two different viewing angles. See also Figure S5.

(D and E) Schematic illustrating (D) t_{on}, the time the autoregulatory element becomes responsive, and (E) t_{off}, the time the early element ceases production. We define t_{off} such that $r(t \geq t_{off}) = 0$, where $r(t)$ is the mRNA production rate of the early element. Before t_{off}, $r(t)$ follows the usual exponential decay observed experimentally with rate $\beta^{-1} = 21$ min. The commitment window $t_{off} - t_{on}$ is the timespan during which both upstream factors and autoactivation dictate Ftz expression, and serves as an estimate for how long the autoregulatory module has to establish a memory of the signal from the early module.

(F) Simulated Ftz concentrations resulting from the timing pictured in (C) and (D).

(G) Contour plot showing what percentage of the subset of analyzed nuclei (n = 21; STAR Methods section "Best predicted nuclei") that reach the high Ftz fate under wild-type conditions still reach that fate as the commitment window $t_{off} - t_{on}$ is varied and t_{on} is delayed relative to the measured −20 min (see text).

(H) Simulated single-nucleus traces of total Ftz for varying values of t_{on} with initial conditions held constant at $r_{-20} = 1.8$ a.u., $R_{-20} = 1.1$ a.u., and $P_{-20} = 2.6$ a.u. The simulations show that the commitment window can cause the transient dynamics to vary quite dramatically. Dashed lines denote the t_{off} (gold) and t_{on} (gray) values used for each plot. The parameters are as in Table S1.

See also Figures S5–S7.

a high Ftz expression state at gastrulation, were predicted to drop to a low Ftz fate (e.g., cell 2 in Figure 7A). No nuclei classified as low Ftz at gastrulation were predicted to express high Ftz after gastrulation. Thus, in principle, the autoregulatory element ensures that the vast majority of cells adopt a fate matching the transient state at gastrulation (Figure 7B).

What are the features of the transient early Ftz dynamics that determine whether the autoregulatory module commits to a high or low fate? We can address this question by looking at the relationship between the initial conditions, which dictate the dynamics of the early module, and the fate predicted by the model. Specifically, because increasing any one of the three initial conditions can only increase Ftz concentration at

subsequent points in time, the regions of parameter space (r_{-20}, R_{-20}, P_{-20}) resulting in high fates are separated from the region of parameters resulting in low fates by a surface called the switching separatrix,[49] so named because if the initial conditions of a cell are above the surface, then the bistable autoregulatory module will switch on.

Figure 7C illustrates the initial conditions for all nuclei at the anterior of stripe 4 alongside the switching separatrix (green surface). The separatrix indicates that a combination of all three initial conditions defines Ftz fate. Particularly noteworthy is that the initial amount of early protein P_{-20} is not the strongest predictor of fate. Cells with comparable levels of P_{-20}, even at the highest concentrations we measured, are partitioned between

ON and OFF fates by the values of r_{-20} and R_{-20} (Figure 7C). Thus, the autoregulatory element does not simply perform an instantaneous readout of Ftz concentration at the time of onset to determine cell fate. Rather, a combination of high initial transcription r_{-20} and high initial mRNA R_{-20}—which together lead to a bump in Ftz concentration *after* the onset of autoregulation—seems to be essential for adopting the high fate.

Given this observation, we asked how long it takes for the autoregulatory element to establish developmental memory of Ftz levels. We posit that this timespan corresponds to the classical notion of a commitment window, defined as the period of time during which a cell integrates information from external factors to decide its fate.[50,51] It can be difficult to access temporal features of development such as the commitment window *in vivo*, in part due to the technical challenge of measuring and systematically manipulating input signals while simultaneously monitoring the resulting gene expression programs in individual cells within intact tissues or organisms.[52,53]

Our mathematical model provided us with a unique opportunity to examine the commitment window by altering the timing of developmental events *in silico*. Because the low Ftz fate at steady state is the default expression state—the autoregulatory module will always produce zero protein in the absence of a transient signal from the early module—the commitment window primarily determines whether the cell has enough time to detect if transient Ftz concentrations are high and, if so, to adopt a trajectory destined for a high steady-state expression fate. Thus, we analyzed only the subset of the best predicted nuclei that were predicted to adopt the high fate according to the switching separatrix analysis (n = 21; Figure 7C, green surface).

We define the commitment window as $t_{off} - t_{on}$, where t_{on} indicates the start of autoregulatory responsiveness (Figure 7D) and t_{off} is the time when the early element ceases transcription (Figure 7E). The commitment window represents the total amount of time during which both the early and autoregulatory modules dictate *ftz* expression, and serves as an estimate for how long the autoregulatory module has to establish a memory of transient Ftz state.

To determine how long of a commitment window allows cells to convert transiently high Ftz concentrations into permanently high Ftz fates, we asked whether our analyzed subset of nuclei still reached the high fate as we systematically varied the commitment window. We solved the dynamical system from Equations 1 and 2 with commitment windows of increasing length and recorded which nuclei reached the high Ftz fate. Our results are reported in Figure 7F in terms of the fraction of nuclei within the subset that adopted the high Ftz fate for each timing condition. For example, assuming $t_{on} \leq -13$ min, a commitment window of 34 min results in 95% of nuclei achieving high steady-state Ftz levels (Figure 7F). Our results reveal that there is a gradual drop-off in the fraction of cells that do not commit to the high fate as the commitment window is shortened or t_{on} is delayed. This suggests that slight temporal perturbations during development are unlikely to cause catastrophic patterning failures in which all cells suddenly adopt the low Ftz fate. Rather, we expect small changes in timing to affect the fates of only a small percentage of cells.

Our analysis of the commitment window suggests that about half an hour suffices for the vast majority of high-fated cells to stably commit to that fate (see also STAR Methods section "Convergence rate estimates and basin of attraction"). Proper fate specification, however, does not guarantee similarity in the temporal trajectories of Ftz concentration, as evidenced by the wide range of dynamics observed in simulated traces for varying t_{on} and t_{off} with the same initial conditions for the early module (Figures 7G and S5D). Thus, if the transient Ftz trajectory, not just its ultimate fate, is instructive for downstream genes, then the need for proper regulation of these genes may place stricter constraints on the relative timing of the early and autoregulatory elements than those that are imposed by the specification of Ftz fate alone.

DISCUSSION

For decades, developmental biologists have used Waddington's landscape to conceptualize cellular decision-making. Under this framework, cells roll down valleys in a predetermined landscape to adopt their ultimate fates. This framework has been repeatedly mathematicized using dynamical systems theory.[54–58] Many of these studies have hypothesized that autoactivation[59] helps establish and maintain binary cell fates through bistability,[1,2] which can be thought of as introducing forks in Waddington's landscape. Though experiments in cell culture and fixed tissue have provided evidence for the bistability of various autoregulatory modules found within gene regulatory networks, until now, these results have not been confirmed by direct examination of dynamics in intact, living embryos.

In this work, we utilized live imaging to quantitatively characterize the dynamics of the fruit fly *ftz* regulatory system *in vivo*. We elucidated tight temporal coordination between the two enhancer elements that regulate *ftz* expression (Figure 3) and combined dynamical systems modeling with biophysical measurements to show that the bistability of the autoregulatory module can maintain otherwise transient expression levels driven by upstream factors (Figure 7). Based on the prevalence of autoregulatory motifs in nature,[5,60] we speculate that the approach employed by the Ftz system to decide cell fate is not limited to fruit flies but might also be widely adopted during development in other organisms.

One of our central discoveries is that *ftz* autoregulation is triggered at a specific developmental time rather than being triggered when Ftz reaches a certain threshold concentration. Recent work has suggested candidates for "timer genes" that are expressed at distinct developmental time points and appear to facilitate the expression of other genes.[36–38,61,62] We speculate that timer genes might also bind the *ftz* autoregulatory element to trigger its responsiveness to Ftz.

We relied on quantitative modeling with no free parameters to provide strong evidence demonstrating that the Ftz autoregulatory module is bistable. Dynamical systems models such as the one employed here are advantageous for this approach since the parameters are biophysically interpretable, which is not true in, for example, more coarse-grained Boolean models of genetic networks.[63] Although the model in the main text is deterministic, in preliminary work we also considered a stochastic chemical reaction network simulated by the Gillespie algorithm, as well as a stochastic differential equation model (STAR Methods section "Stochastic simulations"). Aside from introducing noise to Ftz expression levels, and in contrast to other patterning networks

where noise appears crucial to drive fate determination,[64,65] these models did not exhibit any unique behaviors that better accounted for our experimental observations compared to the deterministic model.

The results presented in this work were derived from experiments paired with mathematical analysis of our theoretical model. The conclusions could be further supported—or challenged—by experiments where Ftz initial conditions are altered through, for example, heat shock or optogenetic approaches. Future research on Ftz autoregulation would also benefit from technological advancements that extend quantitative live imaging capabilities beyond gastrulation in order to monitor Ftz concentrations over extended timescales, from the onset of autoregulation to the final adoption of cellular fate.

A basic assumption of the approach employed here is that the behavior of the whole network can be predicted from the behavior of the parts (modules) in isolation.[66–68] In our model, we divided the early and late populations of Ftz into two separate modules. The early module produces the early protein (P_{early}), which acts as an input to the autoregulatory module responsible for producing the late protein (P_{late}). Positive feedback arises because P_{late} also activates its own expression (Figures 5 and S4). This is not the only way to define the module; for example, if we knew which regulatory factors rendered the autoregulatory element responsive, then we could include those as inputs instead of describing their activity implicitly through the parameter t_{on}. Similarly, if we knew the dynamics of the upstream regulatory factors for the early element, we could replace β, the phenomenological temporal decay in the early transcription rate, with a mathematical expression relating the concentrations of these regulatory factor inputs to the early Ftz transcription rate.

Our representation of the autoregulatory module can predict the fate of *ftz* expression from arbitrary trajectories of early Ftz. As a result, we can predict the effect of modifications to upstream signaling on the resulting gene expression patterns. This allows us to ask what forms of input are appropriate to achieve particular patterning outcomes. Such ability to reverse engineer the process of cellular decision-making could facilitate designing perturbations to manipulate the system, identifying constraints placed on upstream modules by the needs of downstream modules, and analyzing whether biologically evolved signals match those that are mathematically "optimal" for such needs as patterning speed[69] or information transmission.[70] Different methods of generating predictions may be appropriate depending on the types of inputs under consideration. In this paper, the fact that increasing any one of the parameters that define the early Ftz input (r_{-20}, R_{-20}, P_{-20}) increases total Ftz concentration at all points in time (a property known as monotonicity[7,49]) made it possible to analyze our model using a switching separatrix. However, this may not be true for other regulatory systems, as in the case where a gene within a module represses its own production.

Throughout developmental biology, the concept of a commitment window has been repeatedly utilized to describe the amount of time cells need to be exposed to upstream signals in order to decide their developmental fates.[50,51] Our quantitative dynamical systems model enabled us to conduct a detailed examination of this commitment window, and to identify what fraction of cells adopt certain fates as developmental timing is varied. From an engineering perspective, we may consider a gene

expression pattern as an objective that must be achieved with a prescribed level of precision (i.e., as a design specification) and work backward to see what inputs satisfy this requirement. Our approach complements existing work on precision that emphasizes how tightly protein concentrations are controlled[46] and how accurately cells can locate their position by reading out concentrations of upstream factors.[71,72] In particular, the latter approaches indicate what level of precision is actually achieved by a patterning network, while our framing focuses rather on what range of parameters allows a system to attain a predefined level of precision. A combination of the two perspectives could help elucidate what biophysical and evolutionary factors influence stochastic variation in phenotypes, including how precise expression patterns must actually be to produce functional, healthy organisms.

In summary, by turning widespread schematic models of autoactivation modules into precise mathematical statements and experimentally testing the resulting predictions, we have provided support for a widely held hypothesis about how developmental fates are established in embryos. In the future, combining quantitative measurements with precise spatiotemporal perturbations[73] and synthetic reconstitution methods[74] promises to enable yet another iteration of the dialogue between theory and experiment that constitutes the basis of our work, ultimately leading to a predictive understanding of function in developmental networks and the myriad forms and fates to which they give rise.

STAR★METHODS

Detailed methods are provided in the online version of this paper and include the following:

- KEY RESOURCES TABLE
- RESOURCE AVAILABILITY
  - Lead contact
  - Materials availability
  - Data and code availability
- EXPERIMENTAL MODEL AND SUBJECT DETAILS
  - Fly strains/Genotypes
  - Creation of tagged *fushi tarazu* (*ftz*) gene using CRISPR-Cas9
  - Creation of *ftz* early and autoregulatory element reporter
  - Transgenes expressing EGFP and MCP-mCherry
  - Fly lines
- METHOD DETAILS
  - A primer on bistability
  - Embryo preparation and data collection
  - Modeling
  - Parameter estimation
  - Simulations
- QUANTIFICATION AND STATISTICAL ANALYSIS
  - Image processing
  - Numerical analysis and simulations

SUPPLEMENTAL INFORMATION

Supplemental information can be found online at https://doi.org/10.1016/j.cub.2023.06.060.

AUTHOR CONTRIBUTIONS

Conceptualization, J.Z., M.L.P., and H.G.G.; methodology, J.Z., M.L.P., and H.G.G.; resources, J.Z., M.L.P., M.N., and H.G.G.; investigation, J.Z., M.L.P., and H.G.G.; visualization, J.Z., M.L.P., and H.G.G.; funding acquisition, H.G.G.; project administration, H.G.G.; supervision, H.G.G.; writing – original draft, J.Z., M.L.P., and H.G.G.; writing – review & editing, J.Z., M.L.P., and H.G.G.

REFERENCES

1. Zernicka-Goetz, M., Morris, S.A., and Bruce, A.W. (2009). Making a firm decision: multifaceted regulation of cell fate in the early mouse embryo. Nat. Rev. Genet. *10*, 467–477.

2. Soldatov, R., Kaucka, M., Kastriti, M.E., Petersen, J., Chontorotzea, T., Englmaier, L., Akkuratova, N., Yang, Y., Häring, M., Dyachuk, V., et al. (2019). Spatiotemporal structure of cell fate decisions in murine neural crest. Science *364*, eaas9536.

3. Waddington, C. (1957). The Strategy of the Genes (Routledge).

4. Alon, U. (2007). Network motifs: theory and experimental approaches. Nat. Rev. Genet. *8*, 450–461.

5. Peter, I.S., and Davidson, E.H. (2015). Genomic Control Process: Development and Evolution (Academic Press).

6. Ferrell, J.E. (2002). Self-perpetuating states in signal transduction: positive feedback, double-negative feedback and bistability. Curr. Opin. Cell Biol. *14*, 140–148.

7. Angeli, D., Ferrell, J.E., and Sontag, E.D. (2004). Detection of multistability, bifurcations, and hysteresis in a large class of biological positive-feedback systems. Proc. Natl. Acad. Sci. USA *101*, 1822–1827.

8. Graham, T.G.W., Tabei, S.M.A., Dinner, A.R., and Rebay, I. (2010). Modeling bistable cell-fate choices in the *Drosophila* eye: qualitative and quantitative perspectives. Development *137*, 2265–2278.

9. Laslo, P., Spooner, C.J., Warmflash, A., Lancki, D.W., Lee, H.-J., Sciammas, R., Gantner, B.N., Dinner, A.R., and Singh, H. (2006). Multilineage transcriptional priming and determination of alternate hematopoietic cell fates. Cell *126*, 755–766.

10. Kueh, H.Y., Champhekar, A., Nutt, S.L., Elowitz, M.B., and Rothenberg, E.V. (2013). Positive feedback between PU.1 and the cell cycle controls myeloid differentiation. Science *341*, 670–673.

11. Lai, K., Robertson, M.J., and Schaffer, D.V. (2004). The Sonic Hedgehog signaling system as a bistable genetic switch. Biophys. J. *86*, 2748–2757.

12. Bouchoucha, Y.X., Reingruber, J., Labalette, C., Wassef, M.A., Thierion, E., Desmarquet-Trin Dinh, C., Holcman, D., Gilardi-Hebenstreit, P., and Charnay, P. (2013). Dissection of a Krox20 positive feedback loop driving cell fate choices in hindbrain patterning. Mol. Syst. Biol. *9*, 690.

13. Srinivasan, S., Hu, J.S., Currle, D.S., Fung, E.S., Hayes, W.B., Lander, A.D., and Monuki, E.S. (2014). A BMP-FGF morphogen toggle switch drives the ultrasensitive expression of multiple genes in the developing forebrain. PLoS Comput. Biol. *10*, e1003463.

14. Sprinzak, D., Lakhanpal, A., LeBon, L., Santat, L.A., Fontes, M.E., Anderson, G.A., Garcia-Ojalvo, J., and Elowitz, M.B. (2010). *Cis*-interactions between Notch and Delta generate mutually exclusive signalling states. Nature *465*, 86–90.

15. von Dassow, G., Meir, E., Munro, E.M., and Odell, G.M. (2000). The segment polarity network is a robust developmental module. Nature *406*, 188–192.

16. Jaeger, J., Surkova, S., Blagov, M., Janssens, H., Kosman, D., Kozlov, K.N., Manu, Myasnikova, E., Vanario-Alonso, C.E., Samsonova, M., et al. (2004). Dynamic control of positional information in the early *Drosophila* embryo. Nature *430*, 368–371.

17. Lopes, F.J.P., Vieira, F.M.C., Holloway, D.M., Bisch, P.M., and Spirov, A.V. (2008). Spatial bistability generates *hunchback* expression sharpness in the *Drosophila* embryo. PLoS Comput. Biol. *4*, e1000184.

18. Manu, Surkova, S., Spirov, A.V., Gursky, V.V., Janssens, H., Kim, A.R., Radulescu, O., Vanario-Alonso, C.E., Sharp, D.H., Samsonova, M., and Reinitz, J. (2009). Canalization of gene expression in the *Drosophila* blastoderm by gap gene cross regulation. PLoS Biol. *7*, e1000049.

19. Papatsenko, D., and Levine, M. (2011). The *Drosophila* gap gene network is composed of two parallel toggle switches. PLoS One *6*, e21145.

20. Verd, B., Crombach, A., and Jaeger, J. (2017). Dynamic maternal gradients control timing and shift-rates for *Drosophila* gap gene expression. PLoS Comput. Biol. *13*, e1005285.

21. Gutenkunst, R.N., Waterfall, J.J., Casey, F.P., Brown, K.S., Myers, C.R., and Sethna, J.P. (2007). Universally sloppy parameter sensitivities in systems biology models. PLoS Comput. Biol. *3*, 1871–1878.

22. Cotterell, J., and Sharpe, J. (2010). An atlas of gene regulatory networks reveals multiple three-gene mechanisms for interpreting morphogen gradients. Mol. Syst. Biol. *6*, 425.

23. Villaverde, A.F., Henriques, D., Smallbone, K., Bongard, S., Schmid, J., Cicin-Sain, D., Crombach, A., Saez-Rodriguez, J., Mauch, K., Balsa-Canto, E., et al. (2015). BioPreDyn-bench: a suite of benchmark problems for dynamic modelling in systems biology. BMC Syst. Biol. *9*, 8.

24. Wieland, F.-G., Hauber, A.L., Rosenblatt, M., Tönsing, C., and Timmer, J. (2021). On structural and practical identifiability. Curr. Opin. Syst. Biol. *25*, 60–69.

25. Nüsslein-Volhard, C., and Wieschaus, E. (1980). Mutations affecting segment number and polarity in *Drosophila*. Nature *287*, 795–801.

26. Hafen, E., Kuroiwa, A., and Gehring, W.J. (1984). Spatial distribution of transcripts from the segmentation gene *fushi tarazu* during *Drosophila* embryonic development. Cell *37*, 833–841.

27. Wakimoto, B.T., Turner, F.R., and Kaufman, T.C. (1984). Defects in embryogenesis in mutants associated with the antennapedia gene complex of *Drosophila melanogaster*. Dev. Biol. *102*, 147–172.

28. Weiner, A.J., Scott, M.P., and Kaufman, T.C. (1984). A molecular analysis of *fushi tarazu*, a gene in *Drosophila melanogaster* that encodes a product affecting embryonic segment number and cell fate. Cell *37*, 843–851.

29. Hiromi, Y., Kuroiwa, A., and Gehring, W.J. (1985). Control elements of the *Drosophila* segmentation gene *fushi tarazu*. Cell *43*, 603–613.

30. Hiromi, Y., and Gehring, W.J. (1987). Regulation and function of the *Drosophila* segmentation gene *fushi tarazu*. Cell *50*, 963–974.

31. Dearolf, C.R., Topol, J., and Parker, C.S. (1989). Transcriptional control of *Drosophila fushi tarazu* zebra stripe expression. Genes Dev. *3*, 384–398.

32. Pick, L., Schier, A., Affolter, M., Schmidt-Glenewinkel, T., and Gehring, W.J. (1990). Analysis of the *ftz* upstream element: germ layer-specific enhancers are independently autoregulated. Genes Dev. *4*, 1224–1239.

33. Schier, A.F., and Gehring, W.J. (1992). Direct homeodomain–DNA interaction in the autoregulation of the *fushi tarazu* gene. Nature *356*, 804–807.

Current Biology
Article

34. Schier, A.F., and Gehring, W.J. (1993). Analysis of a *fushi tarazu* autoregulatory element: multiple sequence elements contribute to enhancer activity. EMBO J. *12*, 1111–1119.

35. Xiong, W., and Ferrell, J.E. (2007). A positive-feedback-based bistable 'memory module' that governs a cell fate decision. Nature *448*, 1076.

36. Clark, E., and Akam, M. (2016). Odd-paired controls frequency doubling in *Drosophila* segmentation by altering the pair-rule gene regulatory network. eLife *5*, e18215.

37. Clark, E., and Peel, A.D. (2018). Evidence for the temporal regulation of insect segmentation by a conserved sequence of transcription factors. Development *145*, dev155580.

38. Clark, E., Battistara, M., and Benton, M.A. (2022). A timer gene network is spatially regulated by the terminal system in the *Drosophila* embryo. eLife *11*, e78902.

39. Gratz, S.J., Rubinstein, C.D., Harrison, M.M., Wildonger, J., and O'Connor-Giles, K.M. (2015). CRISPR-Cas9 genome editing in *Drosophila*. Curr. Protoc. Mol. Biol. *111*, 1–31.

40. Bothma, J.P., Norstad, M.R., Alamos, S., and Garcia, H.G. (2018). LlamaTags: a versatile tool to image transcription factor dynamics in live embryos. Cell *173*, 1810–1822.e16.

41. Schroeder, M.D., Greer, C., and Gaul, U. (2011). How to make stripes: deciphering the transition from non-periodic to periodic patterns in *Drosophila* segmentation. Development *138*, 3067–3078.

42. Clark, E. (2017). Dynamic patterning by the *Drosophila* pair-rule network reconciles long-germ and short-germ segmentation. PLoS Biol. *15*, e2002439.

43. Garcia, H.G., Tikhonov, M., Lin, A., and Gregor, T. (2013). Quantitative imaging of transcription in living *Drosophila* embryos links polymerase activity to patterning. Curr. Biol. *23*, 2140–2145.

44. Lucas, T., Ferraro, T., Roelens, B., De Las Heras Chanes, J., Walczak, A.M., Coppey, M., and Dostatni, N. (2013). Live imaging of Bicoid-dependent transcription in *Drosophila* embryos. Curr. Biol. *23*, 2135–2139.

45. Lammers, N.C., Galstyan, V., Reimer, A., Medin, S.A., Wiggins, C.H., and Garcia, H.G. (2020). Multimodal transcriptional control of pattern formation in embryonic development. Proc. Natl. Acad. Sci. USA *117*, 836–847.

46. Gregor, T., Tank, D.W., Wieschaus, E.F., and Bialek, W. (2007). Probing the limits to positional information. Cell *130*, 153–164.

47. Mavrakis, M., Rikhy, R., and Lippincott-Schwartz, J. (2009). Plasma membrane polarity and compartmentalization are established before cellularization in the fly embryo. Dev. Cell *16*, 93–104.

48. Edgar, B.A., Weir, M.P., Schubiger, G., and Kornberg, T. (1986). Repression and turnover pattern *fushi tarazu* RNA in the early *Drosophila* embryo. Cell *47*, 747–754.

49. Sootla, A., Oyarzún, D., Angeli, D., and Stan, G.-B. (2016). Shaping pulses to control bistable systems: analysis, computation and counterexamples. Automatica *63*, 254–264.

50. Dalton, S. (2015). Linking the cell cycle to cell fate decisions. Trends Cell Biol. *25*, 592–600.

51. McNeely, K.C., and Dwyer, N.D. (2021). Cytokinetic abscission regulation in neural stem cells and tissue development. Curr. Stem Cell Rep. *7*, 161–173.

52. Bending, D., Prieto Martín, P., Paduraru, A., Ducker, C., Marzaganov, E., Laviron, M., Kitano, S., Miyachi, H., Crompton, T., and Ono, M. (2018). A timer for analyzing temporally dynamic changes in transcription during differentiation *in vivo*. J. Cell Biol. *217*, 2931–2950.

53. Johnson, H.E., and Toettcher, J.E. (2018). Illuminating developmental biology with cellular optogenetics. Curr. Opin. Biotechnol. *52*, 42–48.

54. Wang, J., Zhang, K., Xu, L., and Wang, E. (2011). Quantifying the Waddington landscape and biological paths for development and differentiation. Proc. Natl. Acad. Sci. USA *108*, 8257–8262.

55. Furusawa, C., and Kaneko, K. (2012). A dynamical-systems view of stem cell biology. Science *338*, 215–217.

56. Jaeger, J., and Monk, N. (2014). Bioattractors: dynamical systems theory and the evolution of regulatory processes. J. Physiol. *592*, 2267–2281.

57. Corson, F., and Siggia, E.D. (2017). Gene-free methodology for cell fate dynamics during development. eLife *6*, e30743.

58. Sáez, M., Blassberg, R., Camacho-Aguilar, E., Siggia, E.D., Rand, D.A., and Briscoe, J. (2022). Statistically derived geometrical landscapes capture principles of decision-making dynamics during cell fate transitions. Cell Syst. *13*, 12–28.e3.

59. Crews, S.T., and Pearson, J.C. (2009). Transcriptional autoregulation in development. Curr. Biol. *19*, R241–R246.

60. Alon, U. (2006). An Introduction to Systems Biology (Chapman and Hall/CRC).

61. MacArthur, S., Li, X.Y., Li, J., Brown, J.B., Chu, H.C., Zeng, L., Grondona, B.P., Hechmer, A., Simirenko, L., Keränen, S.V.E., et al. (2009). Developmental roles of 21 *Drosophila* transcription factors are determined by quantitative differences in binding to an overlapping set of thousands of genomic regions. Genome Biol. *10*, R80.

62. Soluri, I.V., Zumerling, L.M., Payan Parra, O.A., Clark, E.G., and Blythe, S.A. (2020). Zygotic pioneer factor activity of Odd-paired/Zic is necessary for late function of the *Drosophila* segmentation network. eLife *9*, e53916.

63. Ay, A., and Arnosti, D.N. (2011). Mathematical modeling of gene expression: a guide for the perplexed biologist. Crit. Rev. Biochem. Mol. Biol. *46*, 137–151.

64. Zhang, L., Radtke, K., Zheng, L., Cai, A.Q., Schilling, T.F., and Nie, Q. (2012). Noise drives sharpening of gene expression boundaries in the zebrafish hindbrain. Mol. Syst. Biol. *8*, 613.

65. Papadopoulos, D.K., Skouloudaki, K., Engström, Y., Terenius, L., Rigler, R., Zechner, C., Vukojević, V., and Tomancak, P. (2019). Control of Hox transcription factor concentration and cell-to-cell variability by an autoregulatory switch. Development *146*, dev168179.

66. Hartwell, L.H., Hopfield, J.J., Leibler, S., and Murray, A.W. (1999). From molecular to modular cell biology. Nature *402*, C47–C52.

67. Bolouri, H., and Davidson, E.H. (2002). Modeling transcriptional regulatory networks. Bioessays *24*, 1118–1129.

68. Del Vecchio, D., Densmore, D., El-Samad, H., Ingber, D., Khalil, A.S., Kosuri, A.D., Lander, S., and Tang, C. (2016). What have the principles of engineering taught us about biological systems? Cell Syst. *2*, 5–7.

69. Pezzotta, A., and Briscoe, J. (2022). Optimal control of gene regulatory networks for morphogen-driven tissue patterning. Preprint at bioRxiv. https://doi.org/10.1101/2022.07.26.501519.

70. Tkačik, G., and Gregor, T. (2021). The many bits of positional information. Development *148*, dev176065.

71. Dubuis, J.O., Tkačik, G., Wieschaus, E.F., Gregor, T., and Bialek, W. (2013). Positional information, in bits. Proc. Natl. Acad. Sci. USA *110*, 16301–16308.

72. Petkova, M.D., Tkačik, G., Bialek, W., Wieschaus, E.F., and Gregor, T. (2019). Optimal decoding of cellular identities in a genetic network. Cell *176*, 844–855.e15.

73. Goglia, A.G., and Toettcher, J.E. (2019). A bright future: optogenetics to dissect the spatiotemporal control of cell behavior. Curr. Opin. Chem. Biol. *48*, 106–113.

74. McNamara, H.M., Ramm, B., and Toettcher, J.E. (2022). Synthetic developmental biology: new tools to deconstruct and rebuild developmental systems. Semin. Cell Dev. Biol. *141*, 33–42.

75. Kim, Y.J., Rhee, K., Liu, J., Jeammet, S., Turner, M.A., Small, S.J., and Garcia, H.G. (2022). Predictive modeling reveals that higher-order cooperativity drives transcriptional repression in a synthetic developmental enhancer. eLife *11*, e73395.

76. Strogatz, S.H. (2018). Nonlinear Dynamics and Chaos (CRC Press).

77. Bothma, J.P., Garcia, H.G., Esposito, E., Schlissel, G., Gregor, T., and Levine, M. (2014). Dynamic regulation of *eve* stripe 2 expression reveals

transcriptional bursts in living *Drosophila* embryos. Proc. Natl. Acad. Sci. USA *111*, 10598–10603.

78. Gillespie, D.T. (2007). Stochastic simulation of chemical kinetics. Annu. Rev. Phys. Chem. *58*, 35–55.

79. Carroll, S.B., and Scott, M.P. (1985). Localization of the *fushi tarazu* protein during *Drosophila* embryogenesis. Cell *43*, 47–57.

80. da Silva, S.M., and Vincent, J.-P. (2007). Oriented cell divisions in the extending germband of *Drosophila*. Development *134*, 3049–3054.

81. Alamos, S., Reimer, A., Westrum, C., Turner, M.A., Talledo, P., Zhao, J., Luu, E., and Garcia, H.G. (2023). Minimal synthetic enhancers reveal control of the probability of transcriptional engagement and its timing by a morphogen gradient. Cell Syst. *14*, 220–236.e3.

STAR★METHODS

KEY RESOURCES TABLE

REAGENT or RESOURCE	SOURCE	IDENTIFIER
Experimental models: Organisms/strains		
D. melanogaster: y[1]w[1118];+; P{w[+mC] = nos:MCP-mCherry-NLS}	Bothma et al.[40]	N/A
D.melanogaster: y[1]w[1118];+; P{w[+mC] = vasa:eGFP}	Kim et al.[75]	N/A
D. melanogaster: y[1]w[1118];+; Ftz-LlamaTag	This study	N/A
D. melanogaster: y[1]w[1118];+; PBac{y[+mDint2]w[+mC] = Ftz-MS2-LlamaTag}VK00033	Bothma et al.[40]	N/A
D. melanogaster: y[1]w[1118];+; PBac{y[+mDint2]w[+mC] = FtzEarly-MS2}VK00033	This study	N/A
D. melanogaster: y[1]w[1118];+; PBac{y[+mDint2]w[+mC] = FtzAutoregulatory-MS2}VK00033	This study	N/A
D. melanogaster: y[1]w[1118];+; PBac{y[+mDint2]w[+mC] = FtzAutoregulatory-MS2-Yellow}VK00033	This study	N/A
Recombinant DNA		
pBPhi-Ftz-MS2-LlamaTag	This study	https://benchling.com/s/seq-x2q87tXdJe9 pqYEOSq9g?m=slm-RjKRHFGZEaS8G81UViCo
pBPhi-FtzEarly-MS2	This study	https://benchling.com/s/seq-T1ED2Irkh 23F57tKLsfw?m=slm-Jz5JH1ORpR5uLQFfEbUM
pBPhi-FtzAuto-MS2	This study	https://benchling.com/s/seq-fe9YzhCIfA2Y k0Lf0q3x?m=slm-pZkVyejK52rJaRg2jPP0
pBPhi-FtzAuto-MS2-Yellow	This study	https://benchling.com/s/seq-bb0p47yyxCk h4q9E626j?m=slm-ddvdLwvG9pengxc50ZFp
pUC57-Ftz-LlamaTag-dsRed	This study	https://benchling.com/s/seq-7GGWtE4Q9 S2WhOMd4ILA?m=slm-WEm4XxVI0m3LN9e0SuQf
pU6-3-gRNA-Ftz-1	This study	https://benchling.com/s/seq-aB8jmNquZreh NgnMjAJz?m=slm-ZjKjLl37mNPTJ7zryjv3
pU6-3-gRNA-Ftz-2	This study	https://benchling.com/s/seq-qo0zUxMPWE COXdDXyLbN?m=slm-Bjt3A3FEXVTwrSzq29dp
pU6-3-gRNA-Ftz-3	This study	https://benchling.com/s/seq-VtOSIvTNGIWCFs Pj2QOu?m=slm-HlvLmtreuEYPthMEN7Gg
Software and algorithms		
MATLAB	Mathworks	https://www.mathworks.com/products/matlab.html
Custom code	This study	https://github.com/GarciaLab/Ftz-Autoregulation-Code

RESOURCE AVAILABILITY

Lead contact
Further information and requests for resources and reagents should be directed to and will be fulfilled by the Lead Contact, Hernan G. Garcia (hggarcia@berkeley.edu).

Materials availability
All plasmids produced and fly lines generated in this paper will be shared by the lead contact upon request.

Data and code availability

- All imaging data reported in this paper will be shared by the lead contact upon request.
- All original code has been deposited on GitHub and is publicly available as of the date of publication.
- Any additional information required to reanalyze the data reported in this paper is available from the lead contact upon request.

EXPERIMENTAL MODEL AND SUBJECT DETAILS

The experimental model used in this study is *Drosophila melanogaster*. Embryos were allowed to develop at room temperature.

Fly strains/Genotypes

The fly lines used in this study were generated by inserting transgenic reporters into the fly genome or by CRISPR-Cas9 genome editing, as described below. See the key resources table for detailed information on the plasmid sequences used in this study.

Creation of tagged *fushi tarazu* (*ftz*) gene using CRISPR-Cas9

Ftz-EGFP-LlamaTag fusion design is based on previously published transgenic line.[40] To tag endogenous *ftz* locus with EGFP-LlamaTag, we used CRISPR-mediated homology-directed repair with donor plasmid synthesized by Genscript. gRNA was designed using the target finder tool from flyCRISPR (https://flycrispr.org), and cloned based on the protocol from Gratz et al.[39] yw;nos-Cas9(II-attP40) transgenic line was used as the genomic source for Cas9 and the embryos were injected and screened by BestGene.

Creation of *ftz* early and autoregulatory element reporter

The *ftz* autoregulatory element sequence was based on the 4.4kb DNA segment described in Hiromi et al.[29] The *ftz* early and autoregulatory element reporters driven by the *ftz* promoter were constructed by combining the respective enhancer sequence with an array of 24 MS2 stem loops inserted into the *ftz* coding sequence *D. melanogaster yellow* gene.[40] The *ftz* autoregulatory element reporter driven by the *eve* promoter was constructed by combining the enhancer sequence with an array of 24 MS2 stem loops inserted into the *D. melanogaster yellow* gene.[40] The constructs were synthesized by Genscript and injected by BestGene into *D. melanogaster* embryos with a Φ C31 insertion site in chromosome 3 (Bloomington stock #9750; landing site VK00033; cytological location 65B2).

Transgenes expressing EGFP and MCP-mCherry

The fly line maternally expressing MCP-mCherry (chromosome 3) was constructed as described in Bothma et al.[40] The fly line maternally expressing vasa-EGFP (chromosome 2) was constructed as described in Kim et al.[75] To simultaneously image protein dynamics using LlamaTags and transcription using MCP-MS2 system, we combined the vasa-EGFP transgene with MCP-mCherry to construct a new line (yw;vasa-EGFP;MCP-mCherry) that maternally expresses both proteins.

Fly lines

To measure Ftz transcription and protein levels simultaneously, we performed crosses to generate virgins carrying transgenes that drive maternal EGFP, MCP-mCherry, the LlamaTagged Ftz locus along with the *ftz* autoregulatory element reporter (yw; $\frac{vasa - EGFP}{CyO}$; $\frac{MCP - mCherry}{FtzAuto - MS2 - Yellow, Ftz - LlamaTag}$). These flies were then crossed with males having both the *ftz* autoregulatory element reporter and the LlamaTagged Ftz locus (yw; +; FtzAuto-MS2-Yellow, Ftz-LlamaTag). This resulted in embryos carrying maternally deposited EGFP, MCP-mCherry, and two copies of the LlamaTagged Ftz locus and *ftz* autoregulatory element reporter.
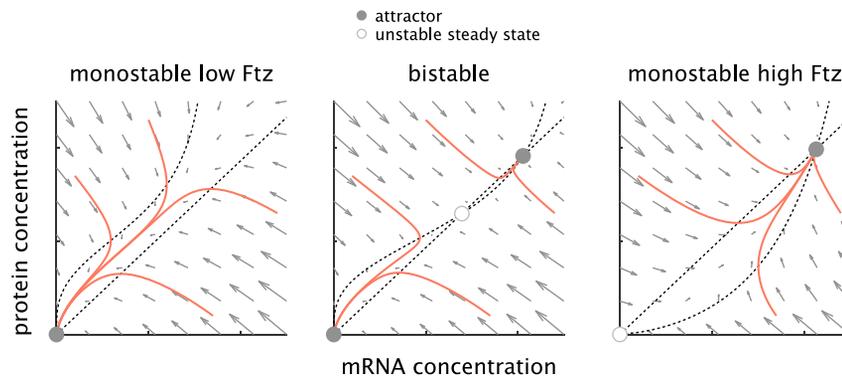
METHOD DETAILS

A primer on bistability

We model *ftz* regulation as a dynamical system represented by ordinary differential equations. Typically, in such models, the rate of change in mRNA and protein concentrations is given by a combination of their synthesis and degradation rates. For example, a model of the *ftz* autoregulatory module in isolation (ignoring regulation by the early element) describes the rate of change in *ftz* mRNA concentration R and protein concentration P as

$$\begin{cases} \dfrac{dR}{dt} = f(P) \, - \, \gamma_R R \\ \dfrac{dP}{dt} = \alpha R \, - \, \gamma_P P \end{cases}. \qquad \text{(Equation 3)}$$

In the first equation, $f(P)$ is the gene regulatory (or input-output) function that describes how input Ftz concentration controls the rate of *ftz* transcription, and γ_R is the *ftz* mRNA degradation rate. Since Ftz promotes its own production, $f(P)$ increases with P. In the second equation, α is the translation rate and γ_P corresponds to the Ftz protein degradation rate.

We can represent this dynamical system using a phase portrait, which is a two-dimensional plot that shows how the trajectory of mRNA and protein concentrations evolves over time. Specifically, the phase portrait has the mRNA and protein concentrations on its axes. At each point in the phase portrait we plug the corresponding mRNA and protein concentrations into Equation 3 in order to calculate $\frac{dR}{dt}$ and $\frac{dP}{dt}$. The values of these derivatives determine how quickly and in which direction the mRNA and protein concentrations will change over a small time period. This direction is encoded in the phase portrait by drawing an arrow. By following arrows throughout the phase portrait, we can qualitatively predict where the trajectory will travel. Hence, given initial concentrations of mRNA and protein, we can predict an entire trajectory by following the arrows.

In the above image, phase portraits for the isolated autoregulatory module described by Equation 3 show how mRNA and protein concentrations change over time. Sample trajectories (red) starting at different points follow the gray arrows encoding $\frac{dR}{dt}$ and $\frac{dP}{dt}$ to converge toward attractors (solid gray circles) and away from unstable steady states (open gray circle). The numerical values of the model parameters determine whether the module is monostable (left and right) or bistable (center), as visualized by the change in the number of intersections of the nullclines (dotted black lines). Parameters for all plots are given in Table S1 except for $c = 0.3$ on the left and $c = 0.65$, $n = 0.7$ on the right, which were chosen for the purpose of illustrating monostability.

We can draw a line on the phase portrait to indicate all points where the mRNA does not change concentration during a small time period (i.e., the arrows are vertical at these points). This line is defined by $\frac{dR}{dt} = 0$ and is called a nullcline. We can similarly identify a nullcline for protein concentration, defined by $\frac{dP}{dt} = 0$ and along which all arrows point horizontally. Trajectories become "stuck" where both $\frac{dR}{dt} = 0$ and $\frac{dP}{dt} = 0$, since concentrations do not change for either molecular species. Such points are called steady states and are found at the intersections of the nullclines. Crucially, the shapes of the nullclines depend on the shape of f as well as the quantitative values of the translation and decay rates, implying that the number of steady states also depends on these parameters.

All trajectories eventually converge to one or more steady states called attractors, so named because they "attract" trajectories toward them. Attractors are stable, meaning that if concentrations are perturbed slightly away from the attractor, they will return to the attractor. Alternatively, a steady state can be unstable, such that, after a small perturbation, the chemical concentrations evolve away from that steady state; in this case the state is not an attractor because trajectories in the vicinity tend to leave rather than approach it. The stability and number of steady states also depend on the system's quantitative parameter values.

For models of the kind we consider here, there are either 1 or 3 steady states, such that the autoregulatory module is either monostable, meaning it possesses one attractor and possibly one unstable steady state, or bistable, meaning it possesses two attractors and one unstable steady state between these attractors. In the monostable case, all trajectories eventually reach the same attractor, whereas in the bistable case, the attractor reached by a given trajectory depends on the initial concentrations of mRNA and protein.

In dynamical systems modeling of ftz regulation of the main text, we discuss how to model *ftz* regulation by a combination of the early and autoregulatory elements, as it occurs in the wild-type embryo. The early element eventually stops driving *ftz* transcription, at which point we can use Equation 3 to describe the evolution of the Ftz mRNA and protein concentrations starting from the values they assumed at the time the early element shut down. Thus, if the autoregulatory module is bistable, then contributions from the early element will determine whether the steady-state Ftz concentration in a given nucleus (trajectory) is high or low, while if the autoregulatory module is monostable, then the steady-state Ftz concentration will always converge toward the same point regardless of the transient activity owing to the early element. Throughout the text, we will refer to the steady-state Ftz concentration that is reached by a trajectory as the Ftz *fate*, to distinguish it from the instantaneous *state* of its concentration at any given point in time.

Embryo preparation and data collection

The embryos were prepared following procedures described in Bothma et al., Garcia et al., and Lammers et al.[40,43,45] Embryos were collected and mounted in halocarbon oil 27 between a semipermeable membrane (Lumox film, Starstedt, Germany) and a coverslip. Confocal imaging on a Zeiss LSM 780 microscope was performed using a Plan-Apochromat 40x /1.4NA oil immersion objective.

EGFP and MCP-mCherry were excited with laser wavelengths of 488 nm (25.0 μW laser power) and 594 nm (15.0 μW laser power), respectively. Fluorescence was detected using the Zeiss QUASAR detection unit. Image resolution was 512 × 512 pixels, with pixel size of 0.231 μm. Sequential z-stacks separated by 0.5 μm were acquired. Specimens were imaged from mid nuclear cycle 14 until the start of gastrulation.

Modeling

Autoregulatory element

We use $R_{early}(t)$ to describe the concentration of *ftz* mRNA transcribed from the early element, which is translated into protein $P_{early}(t)$. We define $R_{late}(t)$ as the *ftz* mRNA transcribed from the autoregulatory element and translated into protein $P_{late}(t)$. The total Ftz in the cell at time t is given by $P_{total}(t) = P_{early}(t) + P_{late}(t)$. The dynamical equations describing the temporal evolution of mRNA and protein are

$$\text{autoregulatory element}: \begin{cases} \dfrac{dR_{late}}{dt} = c\tilde{f}(t, P_{total}(t)) - \gamma_R R_{late}(t) \\ \dfrac{dP_{late}}{dt} = \alpha R_{late}(t) - \gamma_P P_{late}(t) \end{cases}, \quad \text{(Equation 4)}$$

where γ_R and γ_P are the decay rates of mRNA and protein respectively, α is the translation rate, and c is a scaling factor equivalent to the ratio of maximum production rate from the endogenous locus vs. the transgene (where $\tilde{f}$ is measured). Note that $\tilde{f}(t, \cdot)$, the gene regulatory function for the autoregulatory element, is time dependent. Unless otherwise stated, we will assume

$$\tilde{f}(t, P) = \begin{cases} 0, & t < t_{on}, \\ f(P), & t \geq t_{on} \end{cases}, \quad \text{(Equation 5)}$$

where

$$f(P) = \frac{aP^n}{K^n + P^n} + I \quad \text{(Equation 6)}$$

is the sigmoid describing the autoregulatory relationship at maximum amplitude. Using the definition of $P_{total}(t)$ we will then write Equation 4 as

$$\text{autoregulatory element}: \begin{cases} \dfrac{dR_{late}}{dt} = cf(P_{early}(t) + P_{late}(t)) - \gamma_R R_{late}(t) \\ \dfrac{dP_{late}}{dt} = \alpha R_{late}(t) - \gamma_P P_{late}(t) \end{cases}, t \geq t_{on}. \quad \text{(Equation 7)}$$

Thus, $P_{early}(t)$ acts as the sole time-varying input to the autoregulatory element. Since autoregulation does not begin until time t_{on}, the initial conditions for Equation 7 are fixed at $R_{late}(t_{on}) = 0$ and $P_{late}(t_{on}) = 0$.

Early element

From our empirical measurements, we observed that the production rate $r(t)$ of early *ftz* mRNA is well approximated by an exponential decay (Figures 5I and 5J), allowing us to model $R_{early}(t)$ and $P_{early}(t)$ through the dynamical system

$$\begin{cases} \dfrac{dr}{dt} = -\beta r(t) \\ \dfrac{dR_{early}}{dt} = r(t) - \gamma_R R_{early}(t) \\ \dfrac{dP_{early}}{dt} = \alpha R_{early}(t) - \gamma_P P_{early}(t) \end{cases}. \quad \text{(Equation 8)}$$

As before, α is the translation rate and γ_R and γ_P are the decay rates of mRNA and protein.

Because Equation 8 is linear, it can be equivalently written as

$$\frac{d\vec{x}(t)}{dt} = \begin{bmatrix} -\beta & 0 & 0 \\ 1 & -\gamma_R & 0 \\ 0 & \alpha & -\gamma_P \end{bmatrix} \vec{x}(t) = : \mathbf{A}\vec{x}(t), \quad \text{(Equation 9)}$$

where

$$\vec{x}(t) = \begin{bmatrix} r(t) \\ R_{early}(t) \\ P_{early}(t) \end{bmatrix}. \quad \text{(Equation 10)}$$

The analytical solution is then given by

$$\vec{x}(t) = c_1 e^{\lambda_1 t} \vec{v}_1 + c_2 e^{\lambda_2 t} \vec{v}_2 + c_3 e^{\lambda_3 t} \vec{v}_3, \qquad \text{(Equation 11)}$$

where $\lambda_1, \lambda_2, \lambda_3$ are the eigenvalues of A corresponding to eigenvectors $\vec{v}_1, \vec{v}_2, \vec{v}_3$ respectively. In particular,

$$\vec{x}(t) = \begin{bmatrix} 1 \\ \dfrac{1}{\gamma_R - \beta} \\ \dfrac{\alpha}{(\gamma_R - \beta)(\gamma_P - \beta)} \end{bmatrix} c_1 e^{-\beta t} + \begin{bmatrix} 0 \\ 1 \\ \dfrac{\alpha}{\gamma_P - \gamma_R} \end{bmatrix} c_2 e^{-\gamma_R t} + \begin{bmatrix} 0 \\ 0 \\ 1 \end{bmatrix} c_3 e^{-\gamma_P t}, \qquad \text{(Equation 12)}$$

where

$$c_1 = r(t_{on}), c_2 = \left(R_{early}(t_{on}) - \frac{r(t_{on})}{\gamma_R - \beta} \right), c_3 = P_{early}(t_{on}) - \frac{\alpha}{\gamma_P - \gamma_R} c_2 - \frac{\alpha}{(\gamma_R - \beta)(\gamma_P - \beta)} c_1. \qquad \text{(Equation 13)}$$

Thus, the input $P_{early}(t)$ to the autoregulatory element is completely characterized by three parameters $(r(t_{on}), R_{early}(t_{on}), P_{early}(t_{on}))$ corresponding to the initial conditions for Equation 8. Since every term in the solution is multiplied by an exponential that decays in time, all state variables will tend to 0 as t goes to infinity.

Intersection test for bistability

Here, we describe how to use an intersection test to identify steady states such as those introduced in STAR Methods: "A primer on bistability" for our model of the autoregulatory module. To reiterate, our dynamical system Equation 7 is described by

$$\text{autoregulatory element}: \begin{cases} \dfrac{dR_{late}}{dt} = cf(P_{early}(t) + P_{late}(t)) - \gamma_R R_{late}(t) \\ \dfrac{dP_{late}}{dt} = \alpha R_{late}(t) - \gamma_P P_{late}(t) \end{cases}, t \geq t_{on}. \qquad \text{(Equation 14)}$$

Steady states are system states at infinite time. Since we know that $P_{early}(t)$ goes to 0 at long times, the steady states for Equation 7 are equivalent to the steady states of

$$\text{autoregulatory element}: \begin{cases} \dfrac{dR_{late}}{dt} = cf(P_{late}(t)) - \gamma_R R_{late}(t) \\ \dfrac{dP_{late}}{dt} = \alpha R_{late}(t) - \gamma_P P_{late}(t) \end{cases}, \qquad \text{(Equation 15)}$$

which has no time-varying parameters and can therefore be analyzed for steady states by standard methods.

By definition, at steady state the derivative of the different molecules species with respect to time equals zero, allowing us to write

$$\text{autoregulatory element}: \begin{cases} 0 = cf(P_{late}^*) - \gamma_R R_{late}^* \\ 0 = \alpha R_{late}^* - \gamma_P P_{late}^* \end{cases}, \qquad \text{(Equation 16)}$$

where (R_{late}^*, P_{late}^*) is a steady state. Then, we rearrange the bottom equation to get

$$R_{late}^* = \frac{\gamma_P}{\alpha} P_{late}^*, \qquad \text{(Equation 17)}$$

which we plug into the top equation to get

$$0 = cf(P_{late}^*) - \frac{\gamma_R \gamma_P}{\alpha} P_{late}^*. \qquad \text{(Equation 18)}$$

From here, we rearrange terms to recover

$$\gamma_P P_{late}^* = \frac{\alpha c}{\gamma_R} f(P_{late}^*). \qquad \text{(Equation 19)}$$

Hence, the intersections of a line of slope γ_P with the right-hand side give the steady-state late protein concentrations P_{late}^*, from which we can recover R_{late}^* through Equation 17. These intersections can be estimated graphically or through computational methods.

Convergence rate estimates and basin of attraction

In this section, we show our calculation for the local convergence rate to the high Ftz steady state. The convergence rate is an estimate for how quickly a cell approaches the high fate, expressed as the time constant for an exponential decay of the distance between a trajectory and the steady state in the phase space. This section assumes familiarity with linear stability analysis, which is introduced in most nonlinear systems textbooks such as the classic.[76]

Assume we combine Equations 7 and 8 to obtain the full model

$$
\begin{cases}
\dfrac{dr}{dt} = -\beta r(t) \\[2mm]
\dfrac{dR_{early}}{dt} = r(t) - \gamma_R R_{early}(t) \\[2mm]
\dfrac{dR_{late}}{dt} = cf_0(P_{tot}(t)) - \gamma_R R_{late}(t) \\[2mm]
\dfrac{dP_{tot}}{dt} = \alpha(r(t) + R(t)) - \gamma_P P_{tot}(t)
\end{cases}
\quad,
\qquad \text{(Equation 20)}
$$

where $P_{tot}(t) = P_{early}(t) + P_{late}(t)$ and we have used the assumption that

$$
f(t, P) = f_0(P) \qquad\qquad \text{(Equation 21)}
$$

for $t \geq 0$.

The Jacobian of this system about a steady state $(r^*, R_{early}^*, R_{late}^*, P_{tot}^*)$ is

$$
J = \begin{bmatrix}
-\beta & 0 & 0 & 0 \\
1 & -\gamma_R & 0 & 0 \\
0 & 0 & -\gamma_R & cf'(P^*) \\
0 & \alpha & \alpha & -\gamma_P
\end{bmatrix}. \qquad\qquad \text{(Equation 22)}
$$

Since J is a lower triangular block matrix, its eigenvalues are the eigenvalues of the diagonal blocks. The upper left block has eigenvalues

$$
\lambda_1 = -\beta, \lambda_2 = -\gamma_R \qquad\qquad \text{(Equation 23)}
$$

and the lower block has eigenvalues

$$
\lambda_+ = \frac{-(\gamma_P + \gamma_R) + \sqrt{(\gamma_P + \gamma_R)^2 - 4(\gamma_R \gamma_P - \alpha cf'(P^*))}}{2}, \qquad\qquad \text{(Equation 24)}
$$

$$
\lambda_- = \frac{-(\gamma_P + \gamma_R) - \sqrt{(\gamma_P + \gamma_R)^2 - 4(\gamma_R \gamma_P - \alpha cf'(P^*))}}{2}. \qquad\qquad \text{(Equation 25)}
$$

If $\alpha cf'(P^*) > \gamma_R \gamma_P$, the eigenvalue λ_+ is positive, hence the system is bistable and the identified steady state is the unstable middle point. Otherwise the real parts of all eigenvalues are negative and the steady state is (marginally) stable.

Locally to a stable steady state (for which $\alpha cf'(P^*) < \gamma_R \gamma_P$), the convergence rate ξ is determined by the slowest of the decay rates along the eigenvectors, i.e.,

$$
\xi = \min\{b, \gamma_R, |\Re[\lambda_+]|\}, \qquad\qquad \text{(Equation 26)}
$$

where

$$
|\Re[\lambda_+]| < \frac{\gamma_R + \gamma_P}{2}. \qquad\qquad \text{(Equation 27)}
$$

The bound is determined by the point at which the imaginary components of λ_+, λ_- become nonzero. Thus, if $\gamma_P < \gamma_R$, then $|\Re[\lambda_+]| < \gamma_R$, which means that the local convergence rate will be slower than the mRNA decay rate.

The (nonnormalized) eigenvectors associated with each eigenvalue are

$$
\vec{v}_1 = \begin{bmatrix}
-\dfrac{1}{\alpha}(\alpha cf'(P^*) - (\beta - \gamma_P)(\beta - \gamma_R)) \\[2mm]
\dfrac{1}{\alpha(\beta - \gamma_R)}(\alpha cf'(P^*) - (\beta - \gamma_P)(\beta - \gamma_R)) \\[2mm]
-\dfrac{(cf'(P^*))}{\beta - \gamma_R} \\[2mm]
1
\end{bmatrix}, \vec{v}_2 = \begin{bmatrix} 0 \\ -1 \\ 1 \\ 0 \end{bmatrix},
$$

$$\vec{v}_+ = \begin{bmatrix} 0 \\ 0 \\ \frac{1}{\alpha}\left(\gamma_P + \dfrac{-(\gamma_P + \gamma_R) + \sqrt{(\gamma_P + \gamma_R)^2 - 4(\gamma_R\gamma_P - \alpha c f'(P^*))}}{2}\right) \\ 1 \end{bmatrix} = \begin{bmatrix} 0 \\ 0 \\ \frac{1}{\alpha}(\gamma_P + \lambda_+) \\ 1 \end{bmatrix},$$

$$\vec{v}_- = \begin{bmatrix} 0 \\ 0 \\ \frac{1}{\alpha}\left(\gamma_P + \dfrac{-(\gamma_P + \gamma_R) - \sqrt{(\gamma_P + \gamma_R)^2 - 4(\gamma_R\gamma_P - \alpha c f'(P^*))}}{2}\right) \\ 1 \end{bmatrix} = \begin{bmatrix} 0 \\ 0 \\ \frac{1}{\alpha}(\gamma_P + \lambda_-) \\ 1 \end{bmatrix}. \tag{Equation 28}$$

As expected, locally the convergence rate associated with $\lambda_2 = -\gamma_R$ (decay rate of mRNA) has no component in the "protein direction" (i.e., $[0001]\cdot v_2 = 0$), so if we are only interested in the local convergence rate of protein concentration we may ignore λ_2 and instead take

$$\xi_P = \min\{b, |\Re[\lambda_+]|\}. \tag{Equation 29}$$

For the parameters measured in our system, we estimate convergence to the low steady state at the same rate as protein decay and to the high steady state at a rate of approximately 33.6 min, on par with the timescale over which the early element must remain active in order for fate to be appropriately specified.

Parameter estimation
Regulatory function $f(P)$ of the *ftz* autoregulatory element

We calculated the regulatory function ($f(P)$) of the *ftz* autoregulatory element (shown in Figure 4D) for the anterior boundary of stripe 4. To make this possible, we identified the boundary in a manually selected image frame prior to gastrulation by extracting two adjacent columns of cells, each corresponding to high or low Ftz concentration. For each cell, we obtained the MS2 signal, which is a proxy for the instantaneous rate of transcription,[43,45,77] and the Ftz fluorescence for each time point. Next, we binned data points within a specific temporal window into ten quantiles. We averaged the MS2 and Ftz signals belonging to the same quantile, then fit a Hill function to the resulting values to obtain the regulatory function of the *ftz* autoregulatory element within that time window. We repeated the process in four temporal windows (-20 to -15, -15 to -10, -10 to -5, and -5 to 0 min) to obtain the trend shown in Figure 4E.

Translation rate α

To calculate the translation rate, we simultaneously imaged the *ftz* transcription rate and the resulting Ftz concentration in a Ftz-MS2-LlamaTag construct (Figure 5D). We focused on nuclei lacking initial Ftz transcription, meaning that for these nuclei, no MS2 spots were detected prior to the experiment's initiation. For these nuclei, we measured the MS2 signal (see Figure 5E for a sample trace), which is an approximation of the *ftz* mRNA production rate,[40,43,45] and integrated this signal in order to obtain the total amount of mRNA produced[43] (see Figure 5F). This integration was done by solving the differential equation for the mRNA $R(t)$ given by

$$\frac{dR}{dt} = r(t) - \gamma_R R(t), \tag{Equation 30}$$

where $r(t)$ is the transcription rate (i.e., the mRNA production rate reported by MS2 fluorescence), and $\gamma_R = 0.099$ 1/min (see Table S1). An example of a resulting prediction for the amount of mRNA as a function of time is shown in Figure 5F.

Next, we performed a parameter sweep for the translation rate α and, for each value of α, we integrated $R(t)$ to predict the protein dynamics $P(t)$ using the following equation.

$$\frac{dP}{dt} = \alpha R(t) - \gamma_P P(t). \tag{Equation 31}$$

Examples of these predicted protein dynamics traces for different values of α are shown as black lines in Figure 5G.

The translation rate that results in the best fit (Figure 5G, yellow line) is recorded for each nucleus. We then calculated α values for each embryo by averaging best-fitted α for each single cell (Figure 5H). These values are averaged across n = 129 cells (embryo 1) and n = 119 cells (embryo 2), respectively. Then we averaged the resulting value of α between two embryos, giving us $\alpha = 0.082 \pm 0.004$ protein AU /(mRNA AU min) (see Table S1), which is used in our dynamical systems model in the main text.

It is important to note that the correlation between these mRNA dynamics and the protein dynamics, as determined by the translation rate, is independent of which enhancer element drove mRNA expression initially. Furthermore, to calculate α, we utilized a construct that includes both the early and autoregulatory elements rather than focusing solely on the autoregulatory element.

Early element transcriptional activity decay rate β

To determine the decay rate β for mRNA production from the early element, we utilized fluorescence measurements of the early element MS2 reporter construct (Figure 5I). For each embryo, an exponential fit was applied to its average trajectory (Figure 5J). Subsequently, we calculated the mean decay rate across all embryos (see Table S1, n = 2 embryos) for incorporation into the dynamical systems model.

Scaling factor c

We estimated c, the ratio of maximum production rate from the endogenous locus vs. the transgene, by approximating the solution to the dynamical system in Equation 7 between two time points for which we have empirical data. In particular, we began from the experimental observation that $\tilde{f}(t, P)$ plateaus shortly before gastrulation for nuclei with total Ftz levels above about $P_\infty^{thresh} = 1.5 \times 10^6$ a.u. Therefore, for nuclei that satisfy $P_{early}(t) \geq P_\infty^{thresh}$ during this time (Figure S3A), we can approximate the nonlinear system for the autoregulatory element by the following *linear* system

$$\begin{cases} \dfrac{dR}{dt} = cf\left(P_\infty^{thresh}\right) - \gamma_R R(t) \\ \dfrac{dP}{dt} = \alpha R(t) - \gamma_P P(t) \end{cases}, \qquad \text{(Equation 32)}$$

where $f(P_\infty^{thresh})$ is now a constant. This system of equations has an analytical solution given by

$$\begin{cases} R(t) = cR(0)e^{-\gamma_R t} + \dfrac{cf\left(P_\infty^{thresh}\right)}{\gamma_R}\left(1 - e^{-\gamma_R t}\right) \\ P(t) = P(0)e^{-\gamma_P t} + \dfrac{\alpha}{\gamma_P - \gamma_R}\left(R(t) - R(0)e^{-\gamma_P t} - \dfrac{cf\left(P_\infty^{thresh}\right)}{\gamma_P}\left(1 - e^{-\gamma_P t}\right)\right). \end{cases} \qquad \text{(Equation 33)}$$

Rearranging these expressions gives

$$c = \frac{\gamma_P}{f\left(P_\infty^{thresh}\right)\left(1 - e^{-\gamma_P t}\right)}\left(\left(R(t) - R(0)e^{-\gamma_P t}\right) - \frac{\gamma_P - \gamma_R}{\alpha}\left(P(t) - P(0)e^{-\gamma_P t}\right)\right). \qquad \text{(Equation 34)}$$

Note that here $t = 0$ is assigned to the beginning of the time window over which the simulation is performed.

We calculated the solution to Equation 34 for the individual boundary nuclei in the same embryos as used to fit the gene regulatory function (Figure 4D). We restricted our estimations to the 3 min before gastrulation based on personal observations that the prediction accuracy of the simulation of this linearized system tended to fall after ~3 min. We derived the initial conditions $(R(0), P(0))$ from estimates of the late protein obtained by subtracting simulated early protein from the total protein trace (where the autoregulatory element was assumed to begin contributing at -20 min before gastrulation). We estimated c in a windowed approach whereby, for each nucleus, we simulated only over one empirical sample interval (10 s) for all intervals from 3 min before gastrulation (Figure S3B). We pooled all samples for individual time windows across all nuclei (Figures S3C and S3D) and averaged them to give a final estimate of $c \cong 0.45 \pm 0.02$ across the 3 min before gastrulation (where the error range is the standard error).

Simulations
Extracting initial conditions

Initial conditions for all nuclei were drawn from measurements of the endogenous Ftz protein tagged with LlamaTag. In particular, we assumed the autoregulatory element was unresponsive before t_{on} (corroborated by simultaneous measurement of MS2 for the late element transgene in these constructs), such that all protein and mRNA up until 20 min before gastrulation was contributed by the early element. Therefore, our measurements until gastrulation give us the trace $P_{early}(t)$ for $t < t_{on}$.

Protein traces were smoothed before use and provided P_{-20} directly. The early mRNA concentration $R_{early}(t)$ was calculated from the third equation in Equation 1 by plugging in measurements from the smoothed trace to

$$R_{early}(t) = \alpha^{-1}\left(\frac{dP_{early}}{dt} + \gamma_P P_{early}(t)\right), \qquad \text{(Equation 35)}$$

from which R_{-20} could be extracted. The early transcription rate $r(t)$ was then estimated from the derivative of the estimated mRNA trace $R_{early}(t)$ evaluated at $t = -20$ min.

Best predicted nuclei

In order to be assured of the accuracy of our conclusions concerning the dynamics of the commitment process, in Figure 7 we decided to restrict our analysis to sets of nuclei whose simulated trajectories well matched the empirical traces. From our dataset, we identified such "best predicted" nuclei based on the cumulative error between a measured trajectory $\{(R_t, P_t)\}$ at discrete time points t and a simulated trajectory $\{(\widehat{R}_t, \widehat{P}_t)\}$ at the same time points as

$$\epsilon = \sum_t \sqrt{(\widehat{R}_t - R_t)^2 + (\widehat{P}_t - P_t)^2}. \qquad \text{(Equation 36)}$$

From a histogram of the errors (Figure S7A), which was roughly bimodal, we identified a threshold of 7×10^7 to identify the 79 best predicted nuclei out of 118 nuclei total. Some sample traces from these best predicted nuclei are shown in Figure S7B while traces for nuclei with high cumulative error are shown in Figure S7C.

We also calculated the cumulative error when simulations were conducted for a gradual increase in autoregulatory responsiveness described by

$$\hat{f}(t, P) = \left(1 - e^{-\xi(t - t_{on})}f(P)\right), t > t_{on},$$ (Equation 37)

where $f(P)$ is as defined in Equation 6 and $\xi = 0.14$ 1/min corresponds to a half-life of 5 min (from the observation that the autoregulatory element transitions from unresponsive to fully responsive over 10 min; see Figure 4E). The resulting sample traces are shown in Figures S7B and S7C. Compared to the case where we assume that the autoregulatory element becomes active instantaneously at t_{on} (Figure S7A), there was a slight shift in the distribution toward lower error (88 best predicted with the same cutoff as before in Figure S7A), but the binary classification accuracy at gastrulation was the same. Therefore we opted to use $f(P)$ rather than $\hat{f}(t, P)$ for the main analysis.

Whole-embryo simulations

We were curious about how accurately our model, which is based on measurements at the anterior boundary of stripe 4, would predict Ftz state for all nuclei spanning stripes 3, 4 and 5 measured during our experiments. Assuming all nuclei follow the same dynamics as given in Equations 1 and 7, we repeated the analysis from Figure 6 to predict Ftz concentration at gastrulation. We achieved a binary classification accuracy of (74.6%, or 763 of 1036 nuclei). Interestingly, this is worse than the accuracy achieved from thresholding early protein alone (84.3%, or 873 of 1036 nuclei), which is itself comparably accurate to the predictions for the anterior boundary of stripe 4 (with or without the autoregulatory contribution). The bulk of classification errors for the whole-embryo simulations, whether from thresholding full simulations or thresholding early protein alone, were false positives at the posterior boundaries of stripes, as in the example plotted in Figure S5B. This indicates that something differs in the regulation of Ftz at the anterior boundaries of stripes as compared to the posterior boundaries. For example, it has been noted that the posterior, but not the anterior, boundaries of Ftz stripes are repressed by *sloppy paired* (*slp*).[42]

Delaying the onset of responsiveness of the autoregulatory element

From a mathematical standpoint, we can treat a delay in t_{on} as a change in the starting time of the simulation, which introduces a corresponding change to the initial conditions $(r(t_{on}), R_{early}(t_{on}), P_{early}(t_{on}))$ of the early module. In this way, the time at which the trajectory of the early module $(r(t), R_{early}(t), P_{early}(t))$ crosses the switching separatrix is the latest time at which the autoregulatory element can become responsive and still commit a cell to the appropriate (high) fate (Figure S5C). This follows from three conditions: (1) the early element is time invariant, (2) the early element is independent of the autoregulatory module (the same is not true for the autoregulatory module, which takes the output of the early module as its input), and (3) Ftz fate corresponds to the Ftz concentration state at infinite time. (1) and (2) ensure that, even if we delay the autoregulatory element, we can continue to use Equation 1 to simulate early protein by just changing the initial conditions, while (3) ensures that the delayed start of the autoregulatory element will not change the location of the switching surface (which is relative to steady state, not to a transient state of the trajectory at a fixed point in time). Intriguingly, the trajectories of early protein run parallel to the separatrix before converging to cross it in a restricted region of parameter space (Figure S5C).

In Figure 7 we analyze the commitment window by varying t_{off} at the same time as t_{on}. In Figure S5D we report full results for simultaneous variation in t_{on} and t_{off}. The strictness with which cell fate must be specified determines the variation in timing that can be tolerated. For example, if the early element ceases production at or after gastrulation ($t_{off} > 0$), the autoregulatory element can delay responsiveness until -15 min and still guide at least 75% of cells to the appropriate fate. If the early element does not cease production until 20 min, then the autoregulatory element may turn on just after -6 min and still direct 75% of cells to the correct fate. From these results, we see that almost no cells commit to the high fate when $t_{on} > t_{off}$. For this reason, in the main text we always set $t_{off} > t_{on}$.

Stochastic simulations

Stochasticity in gene expression during embryonic development can compromise or improve system function depending on the context.[64,65] We sought to investigate whether stochasticity in gene expression (1) was sufficient to explain the prediction error rates of our deterministic models, and (2) could drive stochastic switching at appreciable rates. We examined these questions using stochastic differential equations (SDEs), assuming that the noise in our data arises solely from stochastic dynamics within the cells rather than from measurement noise. Generally, we expect this method to overestimate the error.

In a stochastic differential equation model, changes in the amount of late RNA dR_{late} and total protein dP_{total} over a time interval dt are given by

$$\begin{cases} dR_{late}(t) = (cf(P_{total}(t)) - \gamma_R R_{late}(t))dt + \sigma_R(R_{late}(t))dW \\ dP_{total}(t) = (\alpha R_{tot}(t) - \gamma_P P_{total}(t))dt + \sigma_P(P_{total}(t))dW, \end{cases}$$ (Equation 38)

where dW is Gaussian with mean 0 and variance dt.[78] The terms $\sigma_R(R_{late})$ and $\sigma_P(P_{late})$ scale the variance of the noise from one time increment to the next.

For this analysis, we used our experimental setup featuring endogenous Ftz-LlamaTag driving an autoregulatory element transgene tagged with MS2 as introduced in Figure 4. Because, over a small time interval where mRNA degradation is negligible, the

MS2 signal reports on the rate of mRNA production, this signal gave us direct access to $dR_{late}(t_i)$ at discrete time points t_i. As a result, we can use this measure of $dR_{late}(t)$ to estimate for the late mRNA $R_{late}(t)$ by integrating the MS2 signal following

$$R_{late}(t_i) = R_{late}(t_{i-1}) + dR_{late}(t_i)(t_i - t_{i-1}) \qquad \text{(Equation 39)}$$

under the assumption that $R_{late}(t_{on}) = 0$ (meaning that the autoregulatory element only becomes responsive at time t_{on}). Since we also have direct measurements of $P_{total}(t)$, this allows us to rearrange Equation 38 so as to estimate the noise contribution $\sigma_R(R_{late}(t))dW$ from

$$\sigma_R(R_{late}(t))dW = dR_{late}(t) - (cf(P_{total}(t)) - \gamma_R R_{late}(t))dt. \qquad \text{(Equation 40)}$$

If we further assume that $R_{early}(t)$ is noiseless and therefore given by the deterministic solution in Equation 12, we can estimate the total mRNA as $R_{total}(t) = R_{early}(t) + R_{late}(t)$. Then, since we have simultaneous measurements of total Ftz P_{total}, we can also rearrange the lower equation in Equation 38 to estimate $\sigma_P(P_{total}(t))dW$ from

$$\sigma_P(P_{total}(t))dW = dP_{total}(t) - (\alpha R_{total}(t) - \gamma_P P_{total}(t))dt. \qquad \text{(Equation 41)}$$

We can perform the above analysis on individual measured traces to produce a large number of sample points of $\sigma_R(R_{late})dW$ and $\sigma_P(P_{total})dW$. With these data we will aim to estimate $\sigma_R(R)$ and $\sigma_P(P)$. We assume the noise characteristics are time invariant, which allows us to pool all samples at all time points and bin them by the corresponding R_{late} or P_{total}. For example, for protein, we treat each protein concentration bin k as a population of samples of $\sigma_P(\overline{P}_{total}^k)dW$ where $\overline{P}_{total}^k$ is the mean of the samples in bin k (Figure S6A). Since we assume dW is normally distributed with variance dt, we divide all sample values by $\sqrt{dt}$ and fit a normal distribution to the resulting distribution within each protein concentration bin (Figure S6B). We found that the variances $\sigma_P(P)^2$ are quite well approximated by a linear relation $\sigma_P(P)^2 = aP + b$ (Figure S6C, right). The mRNA variance was estimated similarly and also found to fit a linear relation (Figure S6C, left). Noise was estimated from all available trajectories, regardless of whether they were part of the stripe 4 anterior boundary.

Having estimated the noise, we investigated whether stochasticity could explain the error rate in our predictions of Ftz expression state at gastrulation. We simulated $N_{sim} = 100$ experiments, each consisting of $N_{nuc} = 118$ nuclei evenly split between those deterministically predicted to be on and those deterministically predicted to be off. Specifically, we found the convex hull defined by the experimentally measured initial conditions for nuclei at the stripe 4 anterior boundary, and drew random initial conditions for the stochastically simulated nuclei from a uniform distribution within this hull. We assigned to each simulated experiment $\frac{N_{nuc}}{2}$ points below the blue surface in Figure 7C and $\frac{N_{nuc}}{2}$ above the surface without replacement (i.e., every nucleus in every simulated experiment has a unique set of initial conditions). Individual stochastic trajectories were generated using the Euler-Maruyama method, with the modification that protein and mRNA concentrations were forcibly lower bounded at 0 (i.e., random fluctuations that would bring concentrations to negative values were capped to instead bring the concentration to zero). Trajectories were simulated for 20 min until gastrulation and thresholded with the same value as for our deterministic simulations (Figure S6D).

From our $N_{sim} = 100$ simulated experiments, we calculated a distribution of error rates given by

$$\frac{\text{total false positives} + \text{total false negatives}}{\text{total number nuclei}}, \qquad \text{(Equation 42)}$$

where we compare the predicted outcomes from deterministic simulations to the "ground truth" of the stochastic simulations.

In Figure S6E we plot the cumulative distribution of error rates for our simulations (black), broken down into false negatives (red) and false positives (green). The dashed vertical lines indicate the experimentally measured error rates with the same color code. Where the vertical lines intersect the corresponding cumulative distributions indicates the probability of measuring an error rate up to that rate. If the system is really described by the stochastic dynamics we have inferred, then the most likely error rates are those that intersect the curves where their slope is highest.

We found that the empirical error rate across 3 embryos was roughly twice that of the most likely error rates from our stochastic simulations corresponding to the middle of calculated cumulative distribution functions (Figure S6E, top), with the majority of errors being false negatives. We knew from observation that one embryo had a large number of false negative predictions, and, interestingly, if we exclude this embryo from analysis, then the empirical error rate aligns well with what the stochastic model predicts to be most likely (Figure S6E, bottom). This result suggests that many of our prediction errors can likely be attributed to stochastic fluctuations.

Having determined that the error of the model in predicting Ftz expression state at gastrulation is comparable to the error expected when considering gene expression stochasticity, we next turned to the question of whether gene expression stochasticity is expected to play a large role in the long-term Ftz fate of cells in which the early element is no longer active. We ran $N = 100$ simulations beginning from the high steady state and calculated the distribution of first-passage times to particular protein values (Figure S6F, left) or to within some Euclidean distance of the opposite steady state (Figure S6F, right). These measures give an approximation of the switching rate depending upon how stringently one defines a threshold for switching.

Both trends indicate that switching from high to low occurs at a much faster rate than low to high, with conservative rates of stochastic switching between the high and low Ftz fates of around 2 hr and between low and high fates of approximately 3 hr. For comparison of timescales, Ftz stripes are no longer experimentally detected before the end of germband extension,[26,79] which occurs

approximately 1.5 h after gastrulation.[80] Thus, we find no strong evidence that stochastic switching should contribute significantly to Ftz stripe patterning.

QUANTIFICATION AND STATISTICAL ANALYSIS

Image processing

Image analysis of live embryo videos was performed based on the protocol in Garcia et al. and Alamos et al.,[43,81] which included nuclear segmentation, spot segmentation, and tracking. In addition, the nuclear fluorescence of Ftz was calculated based on a nuclear mask generated from the MCP-mCherry channel. Ftz concentration for individual nuclei was extracted based on the integrated amount from maximum projection along the z-stack. The GFP background was calculated based on a control experiment and subsequently subtracted from the data.

Numerical analysis and simulations

Numerical analysis and simulations were carried out using custom scripts in MATLAB (2017b). The switching separatrix was estimated using a modification of the algorithm in Sootla et al.,[49] which employs a combination of bisection and random sampling to estimate the upper and lower bounds of the separatrix surface. Stochastic differential equations were simulated using the Euler-Maruyama method.